

MID-INFRARED PROPERTIES OF NEARBY LUMINOUS INFRARED GALAXIES I: SPITZER IRS SPECTRA FOR THE GOALS SAMPLE

S. STIERWALT^{1,2}, L. ARMUS¹, J.A. SURACE¹, H. INAMI^{1,3}, A.O. PETRIC^{1,4}, T. DIAZ-SANTOS¹, S. HAAN^{1,5}, V. CHARMANDARIS^{6,7}, J. HOWELL¹, D.C. KIM⁸, J. MARSHALL¹, J.M. MAZZARELLA⁹, H.W.W. SPOON¹⁰, S. VEILLEUX¹¹, A. EVANS^{2,8}, D. B. SANDERS¹², P. APPLETON¹³, G. BOTHUN¹⁴, C.R. BRIDGE⁴, B. CHAN⁹, D. FRAYER¹⁵, K. IWASAWA¹⁶, L.J. KEWLEY¹², S. LORD⁹, B.F. MADORE¹⁷, J.E. MELBOURNE⁴, E.J. MURPHY¹⁷, J.A. RICH¹², B. SCHULZ¹³, E. STURM¹⁸, V. U¹², T. VAVILKIN¹⁹, K. XU⁹

Draft version October 30, 2018

ABSTRACT

The Great Observatories All-Sky LIRG Survey (GOALS) is a comprehensive, multiwavelength study of luminous infrared galaxies (LIRGs) in the local universe. Here we present low resolution Spitzer IRS spectra covering 5–38 μm and provide a basic analysis of the mid-IR spectral properties observed for nearby LIRGs. In a companion paper, we discuss detailed fits to the spectra and compare the LIRGs to other classes of galaxies. The GOALS sample of 244 nuclei in 180 luminous ($10^{11} \leq L_{\text{IR}}/L_{\odot} < 10^{12}$) and 22 ultraluminous ($L_{\text{IR}}/L_{\odot} \geq 10^{12}$) IR galaxies represents a complete subset of the IRAS Revised Bright Galaxy Sample and covers a range of merger stages, morphologies and spectral types. The majority (>60%) of the GOALS LIRGs have high 6.2 μm PAH equivalent widths ($\text{EQW}_{6.2\mu\text{m}} > 0.4 \mu\text{m}$) and low levels of silicate absorption ($s_{9.7\mu\text{m}} > -1.0$). There is a general trend among the U/LIRGs for both silicate depth and mid-infrared (MIR) slope to increase with increasing L_{IR} . U/LIRGs in the late to final stages of a merger also have, on average, steeper MIR slopes and higher levels of dust obscuration. Together, these trends suggest that as gas & dust is funneled towards the center of a coalescing merger, the nuclei become more compact and more obscured. As a result, the dust temperature increases leading also to a steeper MIR slope. The sources that depart from these correlations have very low PAH equivalent width ($\text{EQW}_{6.2\mu\text{m}} < 0.1 \mu\text{m}$) consistent with their emission being dominated by an AGN in the MIR. These extremely low PAH equivalent width sources separate into two distinct types: relatively unobscured sources with a very hot dust component (and thus very shallow MIR slopes) and heavily dust obscured nuclei with a steep temperature gradient. The most heavily dust obscured sources are also the most compact in their MIR emission, suggesting that the obscuring (cool) dust is associated with the outer regions of the starburst and not simply a measure of the dust along the line of sight through a large, dusty disk. A marked decline is seen for the fraction of high EQW (star formation dominated) sources as the merger progresses. The decline is accompanied by an increase in the fraction of composite sources while the fraction of sources where an AGN dominates the MIR emission remains low. When compared to the MIR spectra of submillimeter galaxies (SMGs) at $z \sim 2$, both the average GOALS LIRG and ULIRG spectra are more absorbed at 9.7 μm and the average GOALS LIRG has more PAH emission. However, when the AGN contributions to both the local GOALS LIRGs and the high- z SMGs are removed, the average local starbursting LIRG closely resembles the starburst-dominated SMGs.

¹ Spitzer Science Center, California Institute of Technology, 1200 E. California Blvd., Pasadena, CA 91125. *e-mail*: sabri-nas@virginia.edu

² Department of Astronomy, University of Virginia, P.O. Box 400325, Charlottesville, VA 22904.

³ National Optical Astronomy Observatory, 950 N. Cherry Ave, Tucson, AZ 85719.

⁴ Department of Astronomy, California Institute of Technology, 1200 E. California Blvd., Pasadena, CA 91125.

⁵ CSIRO Astronomy & Space Science, Marsfield NSW 2122, Australia.

⁶ Department of Physics and ITCPC, University of Crete, GR-71003 Heraklion, Greece.

⁷ IESL/Foundation for Research and Technology - Hellas, GR-71110, Heraklion, Greece and Chercheur Associé, Observatoire de Paris, F-75014, Paris, France.

⁸ National Radio Astronomy Observatory, 520 Edgemont Road, Charlottesville, VA 22903.

⁹ Infrared Processing & Analysis Center, MS 100-22, California Institute of Technology, Pasadena, CA 91125.

¹⁰ Department of Astronomy, Cornell University, Ithaca, NY, 14853.

¹¹ Astronomy Department, University of Maryland, College Park, MD 20742.

¹² Institute for Astronomy, University of Hawaii, 2680 Woodlawn Drive, Honolulu, HI 96825.

¹³ NASA Herschel Science Center, 770 S. Wilson Ave., Pasadena, CA 91125.

¹⁴ Physics Department, University of Oregon, Eugene, OR 97402.

¹⁵ National Radio Astronomy Observatory, P.O. Box 2, Green Bank, WV 24944.

¹⁶ INAF-Observatorio Astronomico di Bologna, Via Ranzani 1, Bologna, Italy.

¹⁷ The Observatories, Carnegie Institute of Washington, 813 Santa Barbara Street, Pasadena, CA 91101.

¹⁸ MPE, Postfach 1312, 85741 Garching Germany.

¹⁹ Department of Physics and Astronomy, SUNY Stony Brook, Stony Brook, NY, 11794.

1. INTRODUCTION

A principal achievement of the Infrared Astronomical Satellite (IRAS) was the discovery of a large population of galaxies whose bolometric luminosities were dominated by emission in the infrared. At the highest luminosities, local ultraluminous infrared galaxies (ULIRGs; $L_{IR} \geq 10^{12}L_{\odot}$) have been heavily studied (Armus et al. 2007; Sanders et al. 1988; Murphy et al. 1996; Spoon et al. 2006; Desai et al. 2007; Rigopoulou et al. 1999; Genzel et al. 1998), and a clear formation picture has been pieced together to explain their extreme emission in the infrared: more than 90% of local ULIRGs are the products of major mergers between molecular gas-rich galaxies. The large amounts of gas that are funneled into the centers of these mergers lead to intense star formation, the feeding of a central AGN, extremely compact reservoirs of molecular gas, and infrared luminosities on the order of ten times their optical luminosities.

While ULIRGs constitute only 3% of the IRAS Revised Bright Galaxy Sample (RBGS; Sanders et al. 2003), at just slightly lower luminosities, luminous infrared galaxies (LIRGs; $10^{11}M_{\odot} \leq L_{IR} < 10^{12}M_{\odot}$) make up almost 1/3 of the IR sources and have formation histories that are far less straightforward. In the local universe, there is evidence that galaxy-galaxy interactions and mergers drive the large IR luminosities in some LIRGs (Sanders & Mirabel 1996) and many high- z submillimeter galaxies (SMGs) show hints of disturbed optical and radio morphologies (Blain et al. 2002; Dasyra et al. 2008). However, at least 20% and as many as 40% of local LIRGs may have no history of major tidal interactions (Howell et al., *in prep*). LIRGs are also represented across the full range of merger stages, unlike ULIRGs which are almost always at the very end stages of coalescing.

Although LIRGs are relatively rare in the local universe, their comoving number density increases by more than 100 times from the current epoch to $z \sim 1$, (Le Floc'h et al. 2005; Magnelli et al. 2009) until LIRGs dominate the total IR energy density at redshifts of $z \sim 1-2$ when star formation in the universe was at its peak (Caputi et al. 2007). Piecing together the formation mechanisms and subsequent evolution of these LIRG systems is thus vital to understanding the processes governing star formation and black hole accretion, the main sources of emitting power in the IR.

The Great Observatories All-sky LIRG Survey (GOALS; Armus et al. 2009) represents a complete subset of the RBGS comprising 180 LIRGs and 22 ULIRGs and aims to provide a multiwavelength understanding of the formation and evolution of local LIRGs as a class of galaxy. As part of the Spitzer Legacy survey, a complete set of IR imaging (Infrared Array Camera (IRAC) at 3.6, 4.5, 5, and 8 μm , and Multiband Imaging Photometer (MIPS) at 24, 70, and 160 μm) and IR spectroscopy at both high and low resolution (Infrared Spectrograph (IRS) from 5-38 μm) is available for the entire sample. In addition, imaging in the near-IR/optical (Hubble Space Telescope NICMOS and ACS; Haan et al. 2011, Kim et al., *in prep*), the UV (Galaxy Evolution Explorer near- and far-UV; Howell et al. 2010), and the X-Ray (Chandra; Iwasawa et al. 2011) are available for large subsets of the sample.

In this paper, we present the mid-infrared (MIR) spec-

tra for 244 galaxy nuclei in the 202 nearby GOALS U/LIRG systems taken with the low resolution module on the Spitzer Infrared Spectrograph (IRS; Houck et al. 2004). The MIR properties derived directly from such a large, complete sample of LIRG spectra will allow us to place these intermediate-luminosity systems into the context of both the extensive previous local ULIRG studies as well as those for lower luminosity, star-forming or starbursting systems (Brandl et al. 2006; Smith et al. 2007b; O'Dowd et al. 2009; Wu et al. 2010).

Full spectral decompositions, including fits to the gas and dust features as well as the SEDs covered by the IRS data, for the entire sample along with the comparison of MIR galaxy properties to those at other wavelengths will be presented in Stierwalt et al. (2013b). The analysis presented here focuses on properties derived directly from the MIR spectra. In Section 2, we present the low resolution MIR spectra observed with the Spitzer IRS Short-Low and Long-Low modules and describe our data reduction methods. In Section 3 we give the distributions of the MIR properties and investigate correlations with L_{IR} and compactness. In Section 4, we follow each MIR property through the merging process, and we place our results into a high redshift context through comparisons to MIR spectra of submillimeter galaxies at $z \sim 2$ in Section 5. Finally, our summary and conclusions are presented in Section 6.

2. OBSERVATIONS & DATA REDUCTION

2.1. The Sample

The GOALS sample consists of 244 galaxy nuclei in 180 luminous and 22 ultraluminous nearby IR galaxies. New spectra were obtained using the staring mode for the IRS Short-Low (SL: 5.5-14.5 μm) and Long-Low (LL: 14-38 μm) modules for 157 galaxies (PID 30323; PI L. Armus). Integration times were determined from nuclear flux densities measured from IRAC and MIPS images and range from 45-120 seconds in SL and 30-120 seconds in LL. Secondary nuclei were targeted when the MIPS 24 μm flux ratio of primary to secondary was ≤ 5 . Archival spectroscopic observations were used for the remaining 45 systems and borrowed most heavily from staring program PIDs 105, 3247, & 20549 and mapping program PIDs 73, 3269, & 30577.

All 202 systems are nearby but cover a range of distances ($15 \text{ Mpc} < D < 400 \text{ Mpc}$) and so the resulting projected IRS slit size varies from source to source. At the median galaxy distance of 100 Mpc, the nuclear spectrum covers the central 1.8 kpc in SL and the central 5.2 kpc in LL.

2.2. Data Reduction

Staring mode spectroscopic data were reduced using the S17 and S18.7 IRS pipelines from the Spitzer Science Center²⁰. For most sources, off-source nods were used to perform background sky subtraction. In the cases of more extended objects, dedicated background pointings were used to determine the sky surface brightness. One dimensional spectra were extracted using the standard extraction aperture and point source calibration modes in SPICE²¹ which employs a tapered extraction aperture

²⁰ <http://ssc.spitzer.caltech.edu/irs/features.html>

²¹ <http://ssc.spitzer.caltech.edu/postbcd/doc/spice.pdf>

that averages roughly to a size of $10''.6 \times 36''.6$ in LL and $3''.7 \times 9''.5$ in SL. After masking bad pixels, multiple nods were averaged to produce the final spectrum.

Of the archival data, 27 spectra were taken in staring mode and were reduced as described above. For the remaining 18 systems, spectra were extracted from low resolution mapping mode data using CUBISM (Smith et al. 2007a). Two-dimensional BCDs were assembled, obvious bad pixels were removed and nuclear spectra were extracted. In two cases (CGCG011-076 and IC1623B), smaller apertures were necessary to avoid other sources in the Long-Low maps, but for most sources 2×5 pixel extraction apertures centered on the galaxy's nucleus were used to resemble as closely as possible the results that would have been achieved with staring mode observations. However, since the tapered aperture used by SPICE cannot be completely reproduced by the square apertures in CUBISM, a further mapping-to-staring-mode correction was applied to all spectra derived from low resolution archival maps. The correction, a multiplicative factor that is a function of wavelength, was derived from NGC6240, a star-forming merger remnant typical of the GOALS sample for which both staring and mapping data were obtained. The correction function varies from 1.3 to 2.7 over SL wavelengths and from 1.7 to 2.3 over LL wavelengths.

The IRAC $8 \mu\text{m}$ (Channel 4) images for six example GOALS galaxy nuclei are shown in Figure 1 with the SL and LL extraction aperture projections overlaid (in the case of staring mode data) or with the CUBISM extraction windows overlaid (in the case of mapping mode data). The low resolution IRS spectrum for each source is also presented along with each MIR image. Spectra for the remainder of the galaxy nuclei, ordered by right ascension, are available as online material and can also be found at <http://goals.ipac.caltech.edu/>. For five galaxies (IIIZw035, IRASF03359+1523, MCG+08-18-013, IRASF17132+5313, and MCG-01-60-022), the archival SL staring mode observations were not centered on the galaxy nucleus, so the SL slit overlays are not shown and the extracted spectra were not used in our analysis. Complete IRS observations were not available for an additional 6 galaxies (no LL spectra: NGC2388, NGC4922, and VV705; no SL spectra: IRASF08339+6517; no IRS data: ESO550-IG025 and IC4518). One galaxy (NGC1068; Howell et al. 2007) saturates the spectrograph and so is also not shown.

2.3. Scale Factors

For each spectrum a break occurs between the SL and LL modules near $14 \mu\text{m}$ due to the larger LL slit, which covers nine times the area covered by the SL slit. The scale factors required to match the SL flux to the LL flux are not applied to the spectra in Figures 1 and A1 but are calculated from the overlap in the SL1 and LL2 modules and presented in Table 1. Scale factors are not given for any source missing either SL or LL data. For a small minority of cases (CGCG448-020, ESO077-IG014, ESO173-G015, ESO255-IG007, ESO343-IG013, ESO440-IG058 (northern nuclei only), IRAS03582+6012, IRASF06076-2139, NGC5653, NGC6090, NGC3690 (western nuclei only), and NGC5256), the scale factor is not given because the placement of the LL slit covered multiple nuclei while the smaller SL slit covered only one.

The median scale factors are 1.22 and 1.70 for the staring and mapping mode data respectively. The larger median scale factor for mapping data most likely reflects a selection bias toward mapping more extended sources. Twelve scale factors are < 1 (i.e. more flux is recovered from SL than from LL), but for all twelve, the scale factors are also > 0.9 and thus represent normal statistical scatter for sources with scale factors near unity. No clear correlation is observed between the scale factors and galaxy distance, but at distances > 300 Mpc, a cutoff that includes 6 sources, the scale factors are all < 1.2 . Similarly, at distances closer than 30 Mpc, there are three GOALS sources that all have scale factors > 1.6 .

The scale factors are applied as a uniform multiplicative factor across the entirety of the SL spectra and thus boost equally the PAH fluxes, the continuum, and the absorption features. Since calculations of the equivalent width of the $6.2 \mu\text{m}$ PAH and the depth of the silicate feature at $9.7 \mu\text{m}$ (EQW_{6.2 μm} and $s_{9.7\mu\text{m}}$; see next section) both use measurements of feature flux relative to the continuum, neither are affected by the scaling of the SL spectrum at these low redshifts. The MIR slopes ($F_{\nu}[30\mu\text{m}]/F_{\nu}[15\mu\text{m}]$) are also unaffected as they only rely on data from the (unscaled) LL portion of the spectrum.

2.4. $s_{9.7\mu\text{m}}$, MIR Slope, & EQW_{6.2 μm}

Silicate depths at $9.7 \mu\text{m}$ ($s_{9.7\mu\text{m}}$) were measured directly from the MIR spectra via: $s_{\lambda} = \log(f_{\lambda}/C_{\lambda})$ where f_{λ} is the measured flux at the central wavelength of the absorption feature and C_{λ} is where the level of the continuum flux would be in the absence of the absorption feature, based on an extrapolation to the surrounding continuum. Thus, a positive value, $s_{\lambda} > 0$, suggests emission at that wavelength and the deeper the absorption, the lower the $s_{9.7\mu\text{m}}$ value.

The fluxes F_{ν} at $15 \mu\text{m}$ and at $30 \mu\text{m}$ were determined from the average of eight data points surrounding each wavelength and were then used to calculate the MIR slope. The wavelength regions used fell within ~ 14.7 - $15.4 \mu\text{m}$ for $F_{\nu}[15 \mu\text{m}]$ and ~ 29.5 - $30.8 \mu\text{m}$ for $F_{\nu}[30 \mu\text{m}]$.

Equivalent widths for the $6.2 \mu\text{m}$ PAH feature (EQW_{6.2 μm}) were measured for each spectrum using the method outlined in Brandl et al. (2006). Briefly, a spline fit was used to estimate the continuum surrounding the $6.2 \mu\text{m}$ PAH feature, and the continuum fit was subtracted from the spectrum. In most cases, anchor points in determining the continuum were set at $5.15 \mu\text{m} < \lambda < 5.31 \mu\text{m}$, $5.8 \mu\text{m} < \lambda < 5.9 \mu\text{m}$, $6.5 \mu\text{m} < \lambda < 6.8 \mu\text{m}$, and $7.1 \mu\text{m} < \lambda < 7.2 \mu\text{m}$, but each spectrum was visually inspected to make sure no features or bad points occurred in these ranges. The PAH flux was then measured using direct integration. The $6.2 \mu\text{m}$ feature was selected for the EQW calculation because, of the five brightest PAH features, it is the least affected by silicate absorption at $9.7 \mu\text{m}$ and $18.5 \mu\text{m}$, and it is not blended with other PAH features. However, in some cases the $6.2 \mu\text{m}$ PAH feature partially overlaps with the absorption feature due to water ice at $6.0 \mu\text{m}$. For those sources found by the spectral fitting to have $\tau_{\text{ice}} > 0$ (see Stierwalt et al. 2013b), the ice absorption was assumed to affect the underlying continuum but not the PAH emission, and the EQW was calculated accordingly. Four galaxies have only upper limits placed on their EQW_{6.2 μm} : IRAS05223+1908,

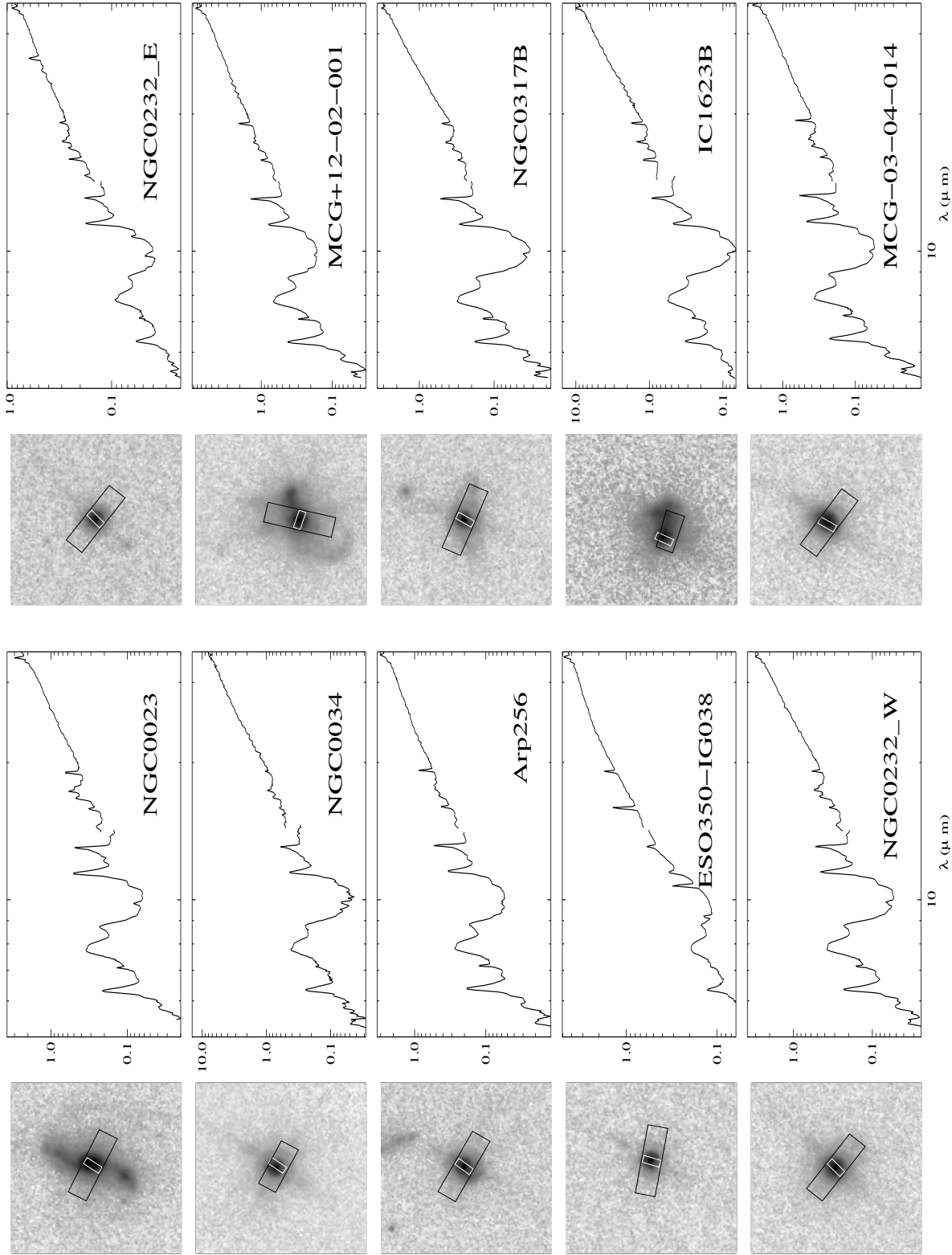


FIG. 1.— IRAC $8\ \mu\text{m}$ (Channel 4) images with Spitzer IRS Short-Low (white) and Long-Low (black) extraction aperture projections and low resolution spectra for six GOALS galaxy nuclei. Each image is $45''$ by $45''$. Spectral flux densities are given in [Jy]. Similar images for the remainder of the sample are available as online material and can also be found at <http://goals.ipac.caltech.edu>.

MCG-03-34-064, NGC4418, and IRAS08572+3015.

2.5. Merger Stages

Merger stages for the entire sample were determined via visual inspection of the IRAC 3.6 μm (Channel 1) images. Each galaxy was assigned one of the following five designations: ‘N’ for nonmergers (no sign of merger activity or massive neighbors), ‘a’ for pre-mergers (galaxy pairs prior to a first encounter), ‘b’ for early-stage mergers (post-first encounter with galaxy disks still symmetric and in tact but with signs of tidal tails), ‘c’ for mid-stage mergers (showing amorphous disks, tidal tails, and other signs of merger activity), or ‘d’ for late-stage mergers (two nuclei in a common envelope). Given the resolution of the IRAC images ($\sim 2''$), late stage mergers can be easily mistaken for nonmergers in the 3.6- μm images. To alleviate this problem, any galaxies classified as nonmergers or early stage mergers in the IRAC images with available higher resolution imaging in the literature that clearly showed signs of a late stage major merger were changed accordingly. We also use the literature to identify spectroscopic pairs which resulted in reclassifying some nonmergers as pre-mergers.

For a subset of 78 GOALS galaxies (all with $\log(L_{IR}/L_{\odot}) > 11.4$), we have additional merger classifications based on available HST B, I, and H-band images. The higher resolution of this imaging enables a more detailed classification system with more finely tuned merger stage designations (stages 0 through 6). These merger stages were already described and presented in Haan et al. (2011), but we reproduce and discuss them here to aid with cross-referencing the two classification schemes.

3. MID-INFRARED PROPERTIES OF NEARBY LIRGS

3.1. LIRG vs ULIRG Distributions

Silicate depths, MIR slopes, PAH equivalent widths, and all associated uncertainties for the GOALS sample, in addition to the SL-to-LL scale factors and merger stages, are presented in Table 1, and the distributions of $EQW_{6.2\mu\text{m},s_{9.7\mu\text{m}}}$, and MIR slope are shown in Figure 2. The $EQW_{6.2\mu\text{m}}$ and $s_{9.7\mu\text{m}}$ parameters are not given for the five sources with off-centered SL spectra, and MIR slopes are not presented for the four sources without available either SL or LL spectra or for the 12 sources for which multiple nuclei are observed within the LL slit.

As shown in Figure 2, the majority of LIRGs (63%) are dominated by PAH emission ($EQW_{6.2\mu\text{m}} > 0.4 \mu\text{m}$), show little to no silicate absorption ($s_{9.7\mu\text{m}} > -1$), and have MIR slopes of $4 < F_{\nu}[30\mu\text{m}]/F_{\nu}[15\mu\text{m}] < 10$. Only six LIRGs have deep silicate absorption with $s_{9.7\mu\text{m}} < -1.75$ (NGC4418, IRAS03582+6012_E, ESO203-IG001, IRASF10038-3338, IRASF12224-0624, and ESO60-IG016). The remainder of the LIRGs show weak to no silicate absorption with a significant fraction (23%) of LIRGs showing silicates in emission at 9.7 μm , including 11% with $s_{9.7\mu\text{m}} > 0.15$. A few of the LIRGs with $s_{9.7\mu\text{m}} > 0$ are likely AGN-dominated ($EQW_{6.2\mu\text{m}} < 0.27 \mu\text{m}$) and thus any absorption at 9.7 μm is filled in by an excess of hot dust. However, most are lower luminosity galaxies with 90% having $\log(L_{IR}/L_{\odot}) < 11.25$. These LIRGs are likely analogous to the unobscured starburst NGC 7714, a galaxy whose IR emis-

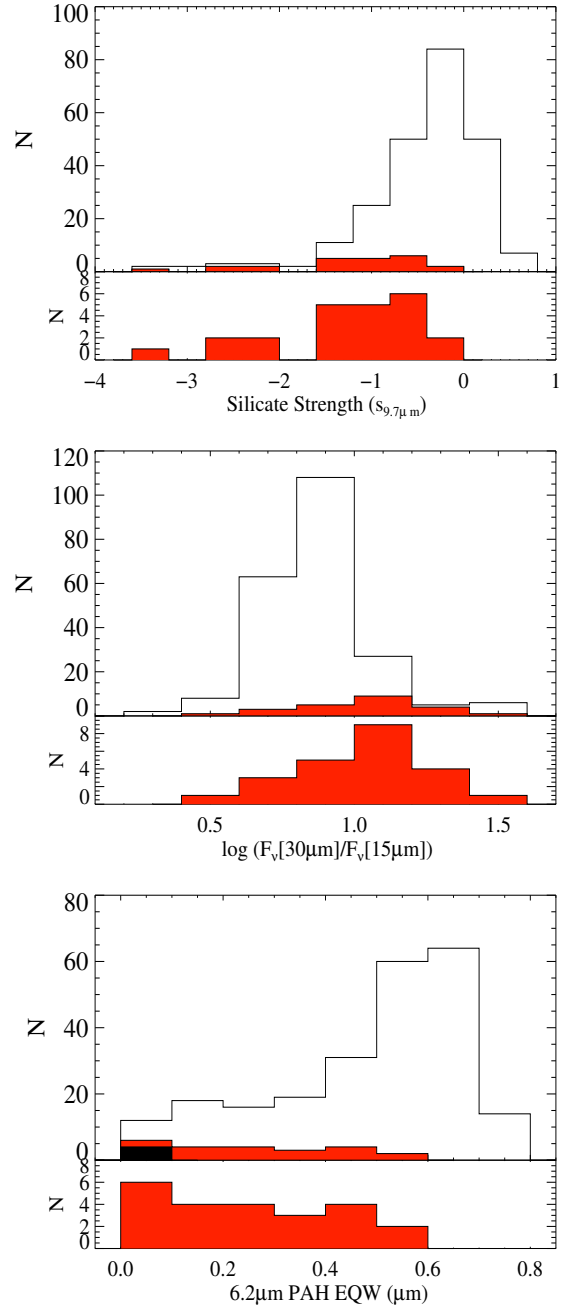


FIG. 2.— Distributions of MIR spectral parameters (upper panels). Top: silicate strength at 9.7 μm , Middle: logarithm of MIR slope, and Bottom: equivalent width of the 6.2 μm PAH feature. On average, GOALS ULIRGs (filled red histograms) have deeper silicate absorption depths, steeper MIR slopes, and lower equivalent widths than the GOALS sample as a whole (white histograms). The lower panel on each plot shows the same GOALS ULIRG distributions with a smaller y-scale. The filled solid black portion of the lowest bin of the $EQW_{6.2\mu\text{m}}$ histogram represents the four sources for which only upper limits are measured.

sion is fueled almost entirely by star formation (Marshall et al. 2007). The silicate strengths in the LIRGs have a median of $s_{9.7\mu\text{m}} = -0.25 \pm 0.58$ and range from the heavily obscured NGC4418 at $s_{9.7\mu\text{m}} = -3.51 \pm 0.09$ to NGC5395, the southern component of the LIRG system Arp84, which shows silicates in emission

($s_{9.7\mu m} = 0.52 \pm 0.07$). Five LIRGs are continuum dominated and show at most only weak PAH or line features (EQW $_{6.2\mu m} < 0.04\mu m$ and $s_{9.7\mu m} > -0.2$; MCG-03-34-064, IRAS05223+1908, NGC1275, NGC7674, and AM0702-601.N).

While the majority of LIRGs favor the high end of the distribution in both EQW $_{6.2\mu m}$ and $s_{9.7\mu m}$, they are found clustered in an intermediate range of MIR slopes with a median of $F_{\nu}[30\mu m]/F_{\nu}[15\mu m] = 7.11 \pm 4.74$. The MIR slopes measured for the LIRGs range from $F_{\nu}[30\mu m]/F_{\nu}[15\mu m] = 2.00 \pm 0.01$ in IRAS05223+1908 which shows a near power-law spectrum in the MIR to $F_{\nu}[30\mu m]/F_{\nu}[15\mu m] = 35.40 \pm 1.38$ in IRAS10173+0828.

For those LIRGs with measurable 6.2 μm PAH EQWs, the values range from EQW $_{6.2\mu m} = 0.005\mu m \pm 0.003\mu m$ for the northeastern component of the LIRG pair IRAS03582+6012 to EQW $_{6.2\mu m} = 0.78\mu m \pm 0.01\mu m$ for the most southeastern of the three galaxies composing the LIRG system IRAS17578-0400. The distribution for all of the GOALS LIRGs has a median of EQW $_{6.2\mu m} = 0.55\mu m \pm 0.18\mu m$. The same median value was found for a sample of lower luminosity starbursting galaxies (Brandl et al. 2006). Tight limits are placed on the EQW for the three LIRGs and one ULIRG without a 6.2 μm PAH detection: IRAS05223+1908 at $<0.043\mu m$, MCG-03-34-064 at $<0.044\mu m$, NGC4418 at $<0.066\mu m$, and IRAS08572+3915 at $<0.081\mu m$.

The GOALS ULIRGs, represented by the solid red histograms in Figure 2, show a clear offset from the LIRGs in their distributions for all three fundamental properties. The ULIRGs have a higher median flux density ratio ($F_{\nu}[30\mu m]/F_{\nu}[15\mu m] = 12.54 \pm 5.41$), a lower median PAH equivalent width (EQW $_{6.2\mu m} = 0.30\mu m \pm 0.17\mu m$), and deeper median silicate absorption ($s_{9.7\mu m} = -1.05 \pm 0.85$). The GOALS ULIRGs span nearly the full range of MIR slopes covered by LIRGs but are not found with EQW $_{6.2\mu m} > 0.52\mu m$ or with $s_{9.7\mu m} > -0.15$. Comparing the derived values for the 22 ULIRGs in GOALS with the larger samples from Spoon et al. (2007) (104 ULIRGs) and Veilleux et al. (2009) (QUEST; 50 ULIRGs), we find that the larger numbers of ULIRGs in these samples result in a larger spread in MIR properties (i.e. 6.2 μm PAH EQWs up to 0.8 μm and silicate depths up to 0.2; Spoon et al. (2007)). However, the median values are consistent with ULIRGs having lower EQW $_{6.2\mu m}$, deeper $s_{9.7\mu m}$, and steeper MIR slope than LIRGs: median EQW $_{6.2\mu m} = 0.15\mu m$ & $s_{9.7\mu m} = -1.47$ (Spoon et al. 2007) and median $F_{\nu}[30\mu m]/F_{\nu}[15\mu m] = 11.6$ (Veilleux et al. 2009).

The results of a Kolmogorov-Smirnov (KS) test give probabilities of $<0.01\%$ that the chance deviations between the distributions of EQW $_{6.2\mu m}$, $s_{9.7\mu m}$, and MIR slope for GOALS LIRGs vs ULIRGs are expected to be larger assuming they are derived from the same parent sample. In other words, the two samples are significantly different. These probabilities decrease by several orders of magnitude when the QUEST and Spoon et al. (2007) ULIRGs are included. When the GOALS ULIRGs are compared to the larger ULIRG samples, the KS test suggests the chance deviations in their distributions in MIR slope, EQW $_{6.2\mu m}$, and $s_{9.7\mu m}$ are expected to be larger with probabilities of 80%, 40%, and 30%, i.e. it is likely the GOALS ULIRGs and the Spoon et al. (2007) &

Veilleux et al. (2009) samples are derived from the same parent sample.

3.2. Correlations with L_{IR}

Figure 3 shows the distributions of $s_{9.7\mu m}$, MIR slope, and EQW $_{6.2\mu m}$ as a function of IR luminosity, L_{IR} . The IR luminosities for all 202 U/LIRG systems were presented in Armus et al. (2009) and derived using the definitions of Sanders & Mirabel (1996)²². In cases of multiple nuclei, the total L_{IR} for the system is divided according to the ratio of the fluxes at 70 μm for each nuclei. In a small number of cases, 70 μm images are not available and so 24 μm flux ratios are used instead.

There is a general trend among the U/LIRGs for both silicate depth and MIR slope to increase with increasing L_{IR} . The sources that depart from these correlations at deep levels of silicate obscuration (top panel) or shallow MIR slopes (middle panel) have, in both cases, very low PAH equivalent width (EQW $_{6.2\mu m} < 0.27\mu m$) and are thus likely dominated by emission from an AGN. Increasingly luminous systems become increasingly dust obscured until a turnover occurs at $s_{9.7\mu m} \sim -1.5$, above which the buried AGN candidates show no further correlation between $s_{9.7\mu m}$ and L_{IR} . As L_{IR} decreases, the MIR slopes flatten until $F_{\nu}[30\mu m]/F_{\nu}[15\mu m] \lesssim 0.5$, below which the relatively unobscured AGN have high L_{IR} given their slopes. ULIRGs have an average EQW $_{6.2\mu m}$ that is lower than that for LIRGs, but sources with a large range of luminosities are found at each equivalent width (lower panel) so there is not a tight correlation between L_{IR} and EQW $_{6.2\mu m}$.

3.3. Disentangling $s_{9.7\mu m}$, MIR Slope, & EQW $_{6.2\mu m}$

To further disentangle the relationship between the 3 main MIR parameters, we examine the $s_{9.7\mu m}$ and EQW $_{6.2\mu m}$ versus MIR slope parameter spaces in Figure 4. The distribution of $s_{9.7\mu m}$ with MIR slope is color-coded by EQW $_{6.2\mu m}$ (panel a) while the distribution of EQW $_{6.2\mu m}$ with MIR slope is color-coded by $s_{9.7\mu m}$ (panel b).

In the majority of LIRGs, star formation dominates the intense MIR emission and the similar conditions in the photodissociation regions resulting in this (PAH-dominated) emission lead to similar MIR properties among the bulk of the GOALS sample. In Figure 4a, the majority of GOALS galaxies, those with EQW $_{6.2\mu m} > 0.27\mu m$ (green squares and blue stars), show a rough correlation between increasing MIR slope and increasing silicate depth (lower $s_{9.7\mu m}$). The starburst galaxies of Brandl et al. (2006) which span mostly luminosities below $10^{11}L_{\odot}$ exhibit a similar relationship between $\tau_{9.7\mu m}$ and $F_{\nu}[30\mu m]/F_{\nu}[15\mu m]$ with the same slope. The trend in Figure 4a suggests that the average dust temperature rises as a consequence of the nuclei becoming more obscured and compact. As the dust temperature increases, the rising portion of the blackbody emission spectrum shifts to shorter wavelengths, and warmer sources have increasingly more flux at 30 μm as seen for the GOALS U/LIRGs with $s_{9.7\mu m} > -1.5$.

²² $L_{IR}/L_{\odot} = 4\pi(D_L[m])^2(F_{IR}[Wm^{-2}])/3.826 \times 10^{26}[Wm^{-2}]$ and $F_{IR} = 1.8 \times 10^{-14}(13.48f_{12\mu m} + 5.16f_{25\mu m} + 2.58f_{60\mu m} + f_{100\mu m}[Wm^{-2}])$

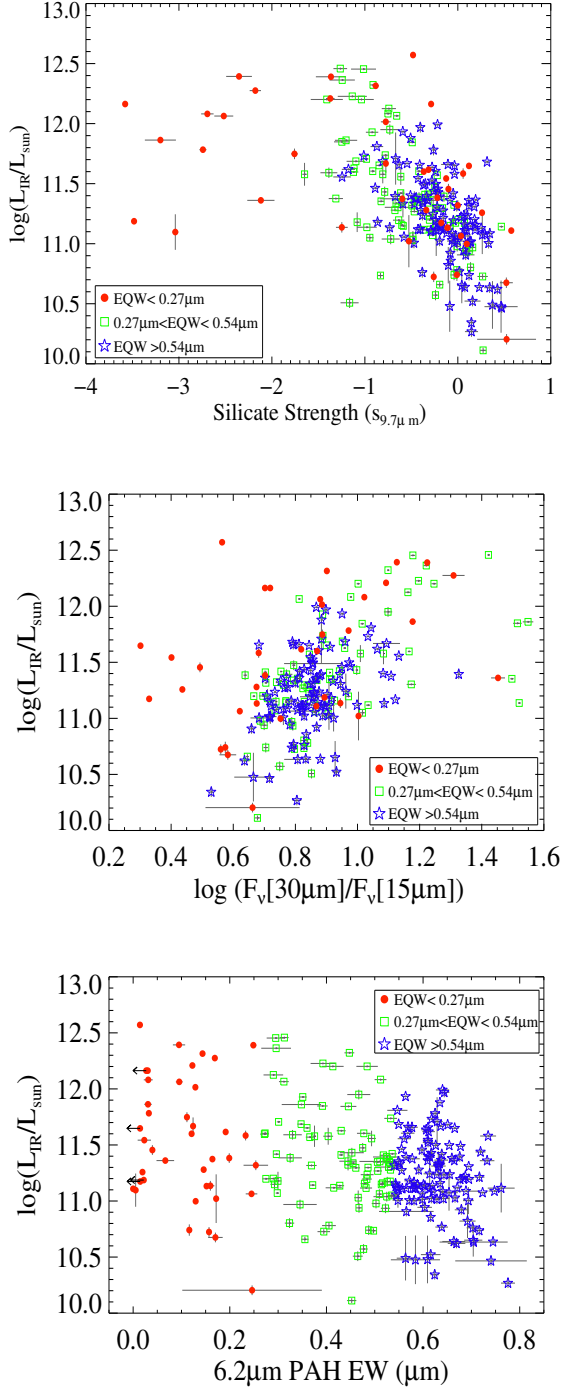


FIG. 3.— Distribution of MIR spectral parameters with L_{IR} color-coded by $\text{EQW}_{6.2\mu\text{m}}$. Top: silicate strength at $9.7\mu\text{m}$, Middle: logarithm of MIR slope, and Bottom: equivalent width of the $6.2\mu\text{m}$ PAH feature. There is a loose trend among LIRGs for increasing silicate depth and MIR slope with increasing L_{IR} . However, LIRGs span nearly the full range of $\text{EQW}_{6.2\mu\text{m}}$ at any given luminosity.

Most of the sources with low PAH equivalent width, however, do not follow these simple trends in MIR properties. In Figure 4a, these low-EQW sources (red circles) are split roughly into two populations: those that are relatively unobscured with shallow MIR slopes and

those heavily obscured sources ($s_{9.7\mu\text{m}} < -1.5$) with steep MIR slopes. A similar split is observed in Figure 4b: for $\text{EQW}_{6.2\mu\text{m}} < 0.27\mu\text{m}$, the heavily obscured sources (purple circles) are found at steeper MIR slopes while the relatively unobscured sources (magenta circles) are found at the shallowest flux density ratios.

An increasingly significant hot dust component from an AGN leads both to a decrease in $\text{EQW}_{6.2\mu\text{m}}$ and to a flatter MIR slope. For the GOALS sources with the strongest, relatively unobscured AGN ($s_{9.7\mu\text{m}} \gtrsim -0.6$; $\text{EQW}_{6.2\mu\text{m}} \lesssim 0.05\mu\text{m}$), an upper limit to the MIR slope can be set at $F_{\nu}[30\mu\text{m}]/F_{\nu}[15\mu\text{m}] < 4$ from both panels in Figure 4. These galaxies (including IRAS05223+1908 and UGC08058) are represented by the red circles in the lower right corner of panel *a* and the magenta circles in the lower left corner of panel *b*. No other sources are found with flatter MIR slopes. This limit agrees with that observed for the starbursts of Brandl et al. (2006) and for the QUEST ULIRGs of Veilleux et al. (2009). Relatively unobscured AGN can thus be identified based on their low MIR flux density ratio alone.

In the most heavily obscured, low EQW galaxies, however, the MIR continuum slopes are steeper due to the buried, hot source. These galaxies (red circles in the left half of Figure 4a and purple circles in Figure 4b) have steep MIR slopes for the same reason sources with $s_{9.7\mu\text{m}} \sim -1.5$ in Figure 4a have steep MIR slopes: most of the warm dust emission is hidden behind a large amount of cooler dust. A comparison to the 5 mJy Unbiased Spitzer Extragalactic Survey (5MUSES; Wu et al. 2010) highlights the difference between the low and high $s_{9.7\mu\text{m}}$ sources at low $\text{EQW}_{6.2\mu\text{m}}$. The 5MUSES sample is $24\mu\text{m}$ selected (indicating the presence of hot dust) but lacks the heavily obscured sources found in GOALS. The distributions for the two samples in Figure 4b are roughly the same (5MUSES is represented by the dashed line although there is significant scatter about this line; see Wu et al. (2010)) - both show the lowest $\text{EQW}_{6.2\mu\text{m}}$ sources have the shallowest MIR slopes - except 5MUSES lacks the obscured low $\text{EQW}_{6.2\mu\text{m}}$ galaxies (purple circles in Figure 4b).

The apparent strength of the $9.7\mu\text{m}$ silicate feature (i.e. the depth of the absorption feature that does not account for any silicate emission, $s_{9.7\mu\text{m}}$) is shown versus $\text{EQW}_{6.2\mu\text{m}}$ in Figure 5 for GOALS LIRGs (open circles) and ULIRGs (red triangles). No galaxies are observed with both high equivalent widths *and* large levels of silicate absorption. However, at low equivalent widths, two distinct branches, similar to those seen by Spoon et al. (2007), emerge that clearly distinguish the lower equivalent width ($\text{EQW}_{6.2\mu\text{m}} < 0.1\mu\text{m}$) sources with minimal to no silicate absorption ($s_{9.7\mu\text{m}} > -0.5$) from those dominated by silicate absorption (heavily obscured sources; $s_{9.7\mu\text{m}} < -1.75$). Sources with intermediate levels of silicate absorption are not found at low equivalent widths.

As shown in Figure 5, the highly absorbed sources are not limited to ULIRGs. At values of $s_{9.7\mu\text{m}} < -1.75$, the GOALS sample includes five ULIRGs (labeled in Figure 5) as well as the dense, compact nascent starburst LIRG NGC4418 (Spoon et al. 2001; Roussel et al. 2003; Evans et al. 2006) and five additional LIRGs that span a large range of LIRG luminosities: IRASF12224-0624 ($\log(L_{\text{IR}}/L_{\odot}) = 11.36$), IRAS03582+6012 ($\log(L_{\text{IR}}/L_{\odot}) = 11.42$), IRASF10038-3338 ($\log(L_{\text{IR}}/L_{\odot}) = 11.78$),

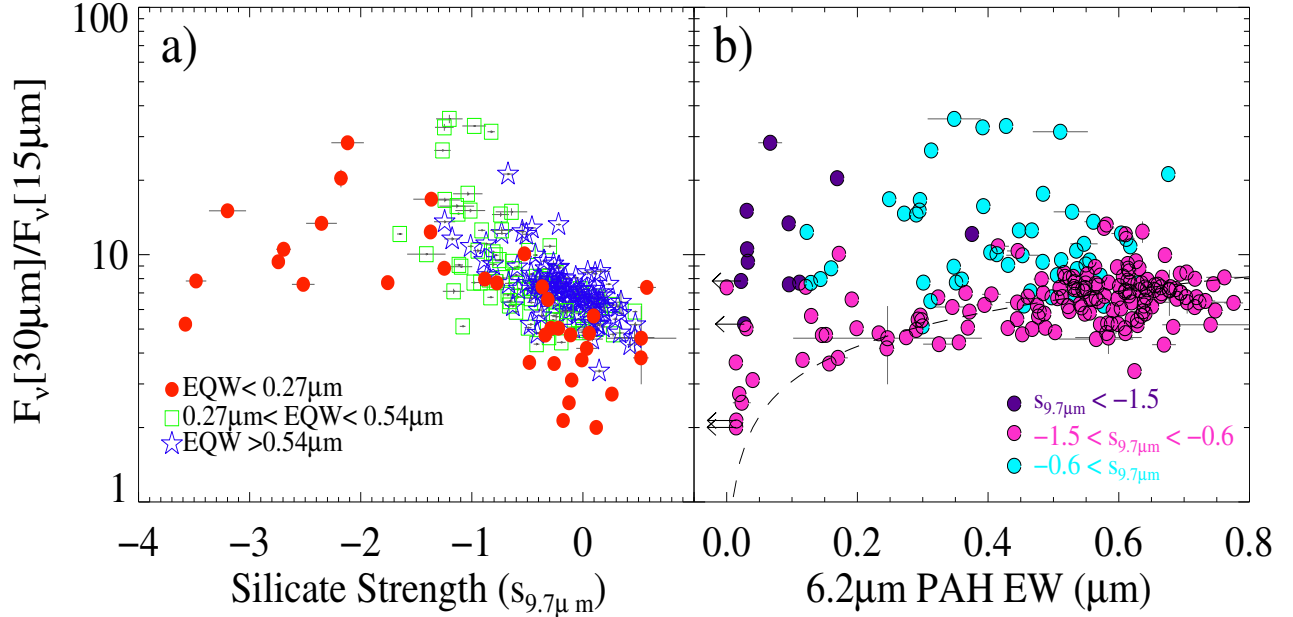


FIG. 4.— Distribution of MIR slope ($F_{\nu}[30\mu\text{m}]/F_{\nu}[15\mu\text{m}]$) versus a) silicate absorption at $9.7\mu\text{m}$ color-coded by $\text{EQW}_{6.2\mu\text{m}}$ and b) $\text{EQW}_{6.2\mu\text{m}}$ color-coded by $s_{9.7\mu\text{m}}$. GOALS sources with $\text{EQW}_{6.2\mu\text{m}} > 0.27\mu\text{m}$ (green squares + blue stars in panel a, right side of panel b) show a rough correlation between increasing silicate depth and increasing MIR slope (a) and follow the correlation between $\text{EQW}_{6.2\mu\text{m}}$ and MIR slope observed in the $24\text{-}\mu\text{m}$ selected 5MUSES sample (dashed line, b; Wu et al. (2010)). At low EQW ($\text{EQW}_{6.2\mu\text{m}} < 0.27\mu\text{m}$; red circles in panel a, left side of panel b), relatively unobscured AGN-dominated sources all have MIR slopes below ~ 4 . However, at the deepest levels of silicate absorption (left side of panel a, purple circles in panel b), the MIR slope is no longer a clear indicator of temperature and so the heavily obscured sources do not follow the trend in panel a, and the location of the $15\text{-}\mu\text{m}$ continuum between the $9.7\mu\text{m}$ and $18.5\mu\text{m}$ absorption features lead to elevated MIR slopes in panel b. Although far less numerous (only 18% of GOALS nuclei have $\text{EQW}_{6.2\mu\text{m}} < 0.27\mu\text{m}$), the lowest equivalent width sources cover a wider range of L_{IR} , MIR slope, and $s_{9.7\mu\text{m}}$ than those sources of higher $\text{EQW}_{6.2\mu\text{m}}$ that make up the majority of the sample.

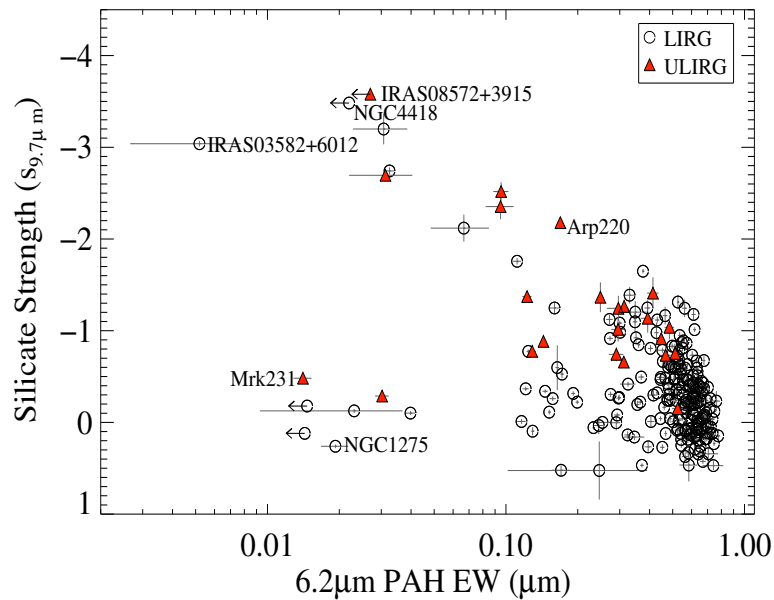


FIG. 5.— Equivalent width of the $6.2\mu\text{m}$ PAH versus silicate strength for the LIRGs (open circles) and ULIRGs (red triangles) of the GOALS sample. The majority ($>60\%$) of the LIRGs are found at $\text{EQW}_{6.2\mu\text{m}} > 0.4\mu\text{m}$ and $s_{9.7\mu\text{m}} > -1.0$, while nearly all ULIRGs have $\text{EQW}_{6.2\mu\text{m}} < 0.5\mu\text{m}$ and $s_{9.7\mu\text{m}} < -0.5$. Sources at low EQW are divided into two distinct branches (silicate-dominated versus continuum-dominated).

ESO60-IG016 ($\log(L_{IR}/L_{\odot}) = 11.82$), and ESO203-IG001 ($\log(L_{IR}/L_{\odot}) = 11.86$).

3.4. Compactness

The most heavily obscured nuclei among the GOALS galaxies are also the most compact: they all show little-to-no MIR emission extending outside of the IRS slit. In Figure 6, the silicate strength is plotted against η , a parameter that represents the fraction of the emission at $24\ \mu\text{m}$ intercepted by the IRS slit:

$$\eta = \log(F_{tot}^{MIPS}[24\mu\text{m}]/F_{slit}^{IRS}[24\mu\text{m}]) \quad (1)$$

where $F_{tot}^{MIPS}[24\mu\text{m}]$ is the total flux of a source as measured from its MIPS $24\ \mu\text{m}$ image (Mazzarella et al., *in prep*) and $F_{slit}^{IRS}[24\mu\text{m}]$ is the flux within the IRS slit derived by convolving the MIPS- $24\ \mu\text{m}$ filter with the low resolution IRS spectrum. The most obscured sources ($s_{9.7\mu\text{m}} < -1.75$) all have $\eta \sim 0$ (i.e. all of the flux measured by the larger MIPS field of view at $24\ \mu\text{m}$ is also recovered within the much smaller IRS slit).

Although distance effects could act to disguise an extended component in comparisons of total versus intra-slit fluxes if all of the obscured sources were the most distant, the median distance for the heavily obscured, low η nuclei is only 60% larger than the median distance for the less obscured sources (190 Mpc vs 115 Mpc) suggesting distance alone cannot be driving the difference in η . Even more importantly, the heavily obscured, low η tail of the distribution in Figure 6 includes the two closest, obscured LIRGs, NGC4418 at 36.5 Mpc and $s_{9.7\mu\text{m}} = -3.51 \pm 0.09$ and NGC3690 at 50.7 Mpc and $s_{9.7\mu\text{m}} = -1.65 \pm 0.02$. Both of these LIRGs would have been easily resolved had they shown any extended MIR emission. Additionally, the existence of galaxies with high η and low $s_{9.7\mu\text{m}}$ with distances well above 100 Mpc indicate that extended sources can still be resolved even at larger distances.

The fraction of resolved emission *within* the IRS slit is also much lower for the obscured sources. The fraction of extended emission ($FEE_{13.2\mu\text{m}}$) is defined by Díaz-Santos et al. (2010) as the fraction of emission within the IRS slit originating outside of the unresolved component (i.e. a point source at that distance). For the most obscured GOALS nuclei, the average $\langle FEE_{13.2\mu\text{m}} \rangle = 0.07$ compared to $\langle FEE_{13.2\mu\text{m}} \rangle = 0.39$ for the remaining (weakly obscured or unobscured) LIRGs. As discussed in detail in Díaz-Santos et al. (2010), such a dramatic difference in FEE between obscured and unobscured nuclei cannot be the result of distance effects alone.

Together the low η , the low $FEE_{13.2\mu\text{m}}$, and their inclusion of nearby sources suggest the nuclei in these heavily obscured sources dominate the $24\text{-}\mu\text{m}$ emission from their parent galaxies, and so the most heavily obscured LIRGs and ULIRGs also have the most compact MIR continuum emission. Given their low $EQW_{6.2\mu\text{m}}$, if extreme levels of obscuration are not simply masking the PAH emission, the higher densities in these nuclei may create an environment where PAH dust grains are not present or the conditions are not appropriate for exciting them (i.e. lacking in photodissociation regions). Alternatively, the low $EQW_{6.2\mu\text{m}}$ may indicate an increase in the continuum flux at $6\ \mu\text{m}$ due to a rise in dust temperature. None of the low η , high $s_{9.7\mu\text{m}}$ nuclei are observed

to be [NeV] emitters (Petric et al. 2011), most likely because their large optical depths obscure any line emission that would be present at $14.3\ \mu\text{m}$.

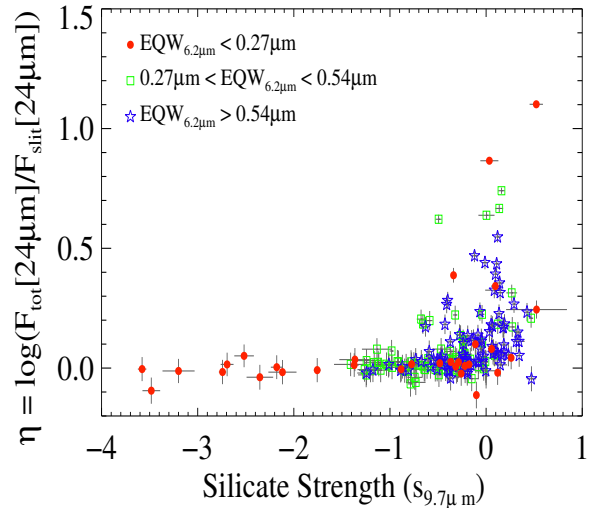


FIG. 6.— Silicate strength versus η , a measure of the total-to-slit flux ratio at $24\ \mu\text{m}$. GOALS LIRGs and ULIRGs are color coded by $6.2\ \mu\text{m}$ PAH equivalent width with low equivalent width (AGN-dominated) sources ($EQW_{6.2\mu\text{m}} < 0.27\ \mu\text{m}$) represented by red circles and high equivalent width (starburst-dominated) sources ($EQW_{6.2\mu\text{m}} > 0.54\ \mu\text{m}$) represented by blue stars. Intermediate EQW (composite) sources are shown by orange ($0.27\ \mu\text{m} < EQW_{6.2\mu\text{m}} < 0.41\ \mu\text{m}$) and green ($0.41\ \mu\text{m} < EQW_{6.2\mu\text{m}} < 0.54\ \mu\text{m}$) squares. Heavily obscured sources have no extended component to their $24\ \mu\text{m}$ emission ($\eta \sim 0$).

4. TRACING MIR PROPERTIES THROUGH MERGER STAGE

In Figure 7, silicate strength, MIR slope, and PAH equivalent width are traced through merger stage for GOALS galaxies. To look for subtle differences in MIR properties throughout the merging process, we focus on only those sources that have HST classifications (column 11 in Table 1). Since this subset contains only six galaxies with no indication of a merger (stage 0), we include all of the nonmergers (Stage N) from the IRAC-based classifications (column 10 in Table 1) to derive a more secure median for each spectral property. Although the HST data samples only LIRGs with $\log(L_{IR}/L_{\odot}) > 11.4$, the dense sampling of merger stages made possible by the deep, high spatial resolution optical and NIR images provides a much finer look at the spectral changes along the merger sequence. Mean values for each merger stage clipped at 3σ are shown in red with their associated standard deviations.

As the mergers progress and gas & dust is funneled towards the center, galaxies become on average more obscured with steeper MIR slopes. Silicate depths of $s_{9.7\mu\text{m}} \lesssim -1$ are only reached at merger stages of 3 and later. No LIRG systems in merger stage 1 have $F_{\nu}[30\mu\text{m}]/F_{\nu}[15\mu\text{m}] > 1$, while the average MIR slope is > 1 for the later stages 4-6. These two results agree with several studies finding higher L_{IR} at later merger stages since, as shown in Figure 3, increasing MIR slope and silicate depth are also linked to higher L_{IR} in LIRGs. As merging galaxies coalesce, the nuclei become more

compact and more obscured, and, as a result, the dust temperature increases leading to a steeper MIR slope as discussed in Section 3.

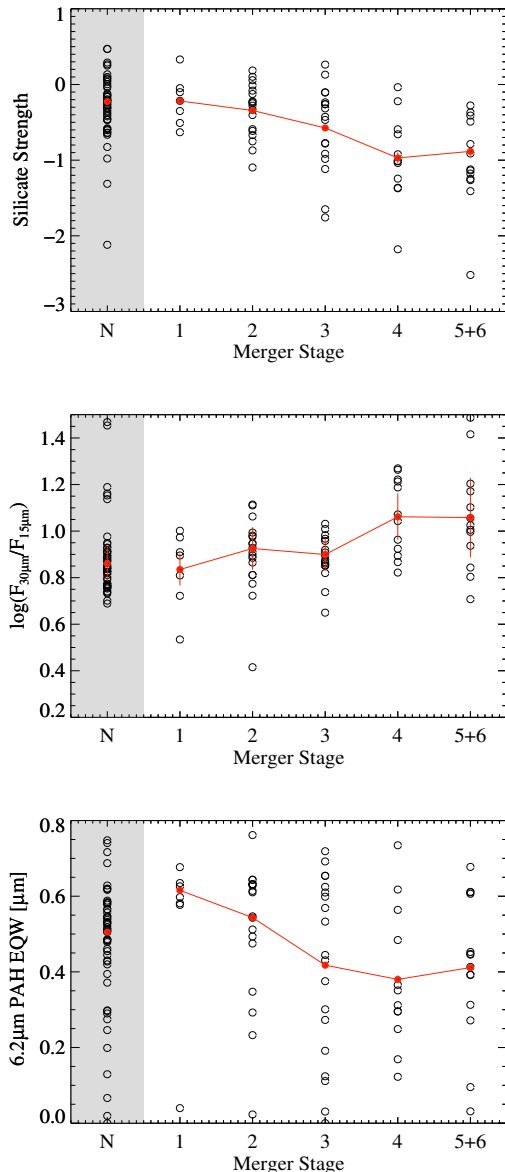


FIG. 7.— MIR properties of GOALS galaxies traced through merger stage. Top: silicate strength ($s_{9.7\mu m}$), Middle: MIR slope ($\log(F_{\nu}[30\mu m]/F_{\nu}[15\mu m])$), and Bottom: $EQW_{6.2\mu m}$. Mergers (Stages 1-6) are represented by the 78 GOALS galaxies for which high resolution HST imaging is available (Haan et al. 2011, ; see Column (11) in Table 1). Nonmergers (Stage N) are classified using IRAC 3.6 μm images and the literature (see Section 2.5 for details). Mean values for each merger stage clipped at 3σ are shown in red with their associated standard deviations.

There is some indication that lower PAH equivalent widths are favored at later merger stages but this is mostly dominated by the fact that only starburst-dominated galaxies ($EQW_{6.2\mu m} > 0.54\mu m$) are observed in stage 1. (The one exception is southern component of the LIRG system AM0702-601.) For all other merger stages, the full range of $EQW_{6.2\mu m}$ is observed.

A clearer link between PAH equivalent width and merger stage is observed when galaxies are binned by their $EQW_{6.2\mu m}$ (and thus the likely AGN contribution to the MIR). In Figure 8 the LIRGs are divided into three $EQW_{6.2\mu m}$ bins indicating AGN dominated sources (red circles), composite sources (green squares), and starbursts (blue stars). Starbursts clearly play a dominant role at early merger stages as was also shown by Petric et al. (2011) and Haan et al. (2011), but the decline in the starburst contribution is not balanced by an increase in AGN-dominated sources. The contribution from LIRGs with an AGN dominating in the MIR stays at a roughly constant fraction throughout the merger process, but *composite* sources (i.e. the weaker AGN that are not yet entirely dominant over star formation in the MIR) show a marked increase at later merger stages. This may indicate that the timescales for the AGN to begin to dominate the MIR emission are longer than the merger timescale (a few hundred million years). In both Figures 7 and 8, the nonmerging LIRGs cover nearly the full range of every MIR property investigated.

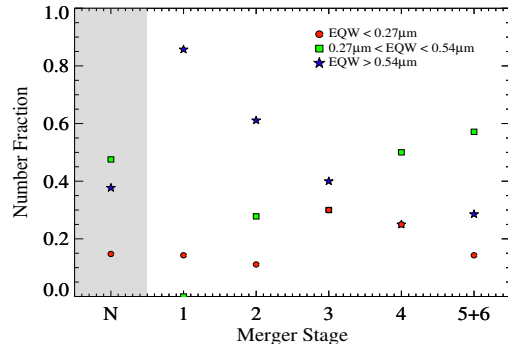


FIG. 8.— Overall AGN fraction (as determined by EQW of the $6.2\mu m$ PAH) traced through merger stage for the GOALS sample. Merger stages are classified as described in Figure 7. A marked decline is seen for the fraction of high EQW (star formation dominated; blue stars) sources as the merger progresses. This decline is accompanied by an increased contribution not from the strongest AGN (red circles) which remain low but from the composite sources (i.e. weaker AGN that are not yet entirely dominant over star formation in the MIR; green squares).

5. COMPARISONS TO SUBMILLIMETER GALAXIES

The dust-enshrouded, strongly starbursting nature of LIRGs makes them obvious candidates for possible local analogs to the dusty submillimeter galaxies (SMGs) that make a significant contribution to the global star formation rate density at higher redshifts. In Figure 9, we compare different subsets of the GOALS MIR spectra with the average SMG spectra from Menéndez-Delmeestre et al. (2009) (hereafter M09) derived from a sample of 24 SMGs at redshifts of $0.65 < z < 3.2$. All average spectra for both the LIRGs and the SMGs are normalized at $6.8\mu m$. In agreement with the conclusions of Desai et al. (2007) and M09, the average local ULIRG spectrum (red line in Figure 9a) is more absorbed than the average SMG spectrum (black line) but has weaker PAH emission. Although GOALS LIRGs are less obscured than ULIRGs on average, the average LIRG spectrum (dashed line)

is still more absorbed than the average SMG while also showing stronger PAH emission at $6.2\ \mu\text{m}$, $7.7\ \mu\text{m}$, and $11.3\ \mu\text{m}$. Even when the nuclear emission of galaxies is removed, the spectrum of the extended component of LIRGs does not resemble that of the total SMG composite (Díaz-Santos et al. 2011). The average local starburst (blue line; Brandl et al. 2006) shows a similar level of silicate absorption but much stronger PAH emission compared to the average SMG.

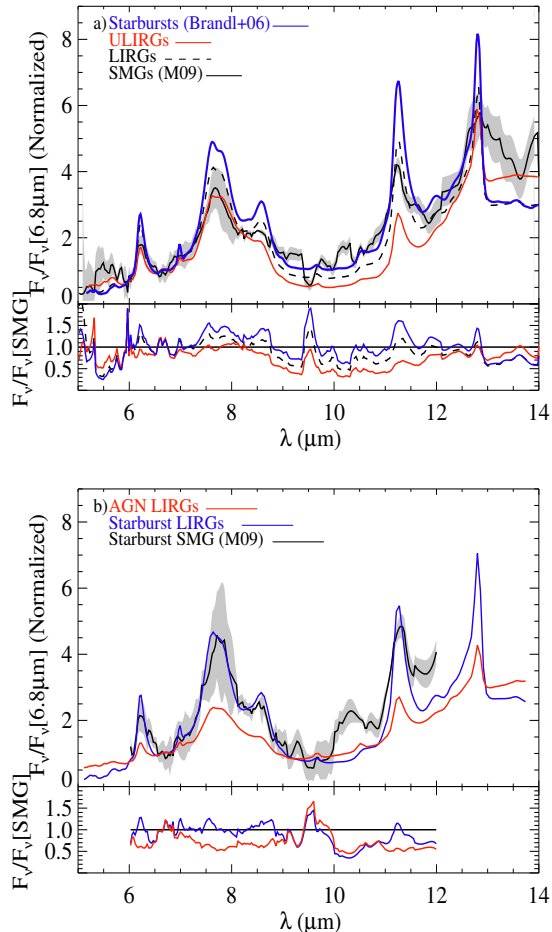


FIG. 9.— Comparison of GOALS average LIRG and ULIRG spectra to average submillimeter galaxy spectra from Menéndez-Delmestre et al. (2009): a) the composite SMG spectrum (black) is less obscured than the average ULIRG (red) and the average LIRG (dashed) but has weaker PAH emission than local starbursts (blue). b) after removing the AGN-dominated systems from both the average SMG and the average LIRG, the average starburst SMG spectrum (black) is well-represented by the starburst LIRGs ($\text{EQW}_{6.2\ \mu\text{m}} > 0.54\ \mu\text{m}$; blue) but not the AGN-dominated LIRGs ($\text{EQW}_{6.2\ \mu\text{m}} < 0.27\ \mu\text{m}$; red) with the exception of a feature at $\sim 10.5\ \mu\text{m}$. All average spectra are normalized at $\lambda = 6.8\ \mu\text{m}$ and the shaded gray area represents the $1\text{-}\sigma$ standard deviation to the averaged SMG spectrum. Residuals are shown in the bottom panels.

The fraction of MIR emission attributed to AGN overall for the GOALS LIRGs is only 12% (Petric et al. 2011), and M09 observed a contribution of $< 32\%$ from AGN to the total bolometric luminosity in SMGs. However, as seen in Figures 1 and A1, those sources dominated by AGN have MIR spectra that are vastly different from

those with strong PAH emission. The low equivalent width sources (i.e. those with MIR emission that is most likely AGN-dominated) also show a larger scatter in their MIR properties, as discussed in Section 3. To reduce possible confusion caused by this AGN contribution, we also compare the average SMG spectrum for only those SMGs without AGN indicators in the MIR (i.e. starburst SMGs with $\text{EQW}_{7.7\ \mu\text{m}} > 1\ \mu\text{m}$ & $\alpha_{\text{MIR}} < 0.5$; M09) to average LIRG spectra with and without an AGN contribution in Figure 9b.

The average AGN-dominated LIRG spectrum (LIRGs with $\text{EQW}_{6.2\ \mu\text{m}} < 0.27\ \mu\text{m}$; red line) clearly does not resemble the average starburst SMG (solid black line). However the average starburst-dominated LIRG spectra ($\text{EQW}_{6.2\ \mu\text{m}} > 0.54\ \mu\text{m}$; blue line) is a better match to the average starburst SMG. All three average spectra agree within 15% below $10\ \mu\text{m}$ (see the residuals in the lower panel).

Between $10\text{--}11\ \mu\text{m}$, all three average LIRG spectra in Figure 9b agree closely, but no subset of the GOALS LIRGs or ULIRGs reproduces the emission feature observed in the average starburst SMG spectrum near $10.5\ \mu\text{m}$. Although the feature is also not detected in the average (low resolution) local starburst spectrum (see Figure 9a), both the [SIV] emission line at $10.51\ \mu\text{m}$ and a PAH feature at $10.60\ \mu\text{m}$ are clearly seen in the average of the high resolution IRS spectra of the same starburst sample (see Figure 4 of Bernard-Salas et al. 2009). The feature detected in the low resolution SMG spectra is likely a blend of these two features (Sturm et al. 2000; Bernard-Salas et al. 2009; Smith et al. 2007b), but may be dominated by the PAH feature emission since it remains faint and unresolved at low resolution. Bernard-Salas et al. (2009) also detect a third feature at $10.75\ \mu\text{m}$ that they associate with PAH emission due to its close correlation with the $11.3\ \mu\text{m}$ PAH which may contribute to the emission in the SMGs.

6. SUMMARY & CONCLUSIONS

We presented low resolution IRS spectra for 244 galaxy nuclei in the GOALS sample of 180 LIRGs and 22 ULIRGs. The GOALS galaxies cover a range of spectral types, silicate strengths, and merger stages, and represent a complete subset of the IRAS Revised Bright Galaxy Sample. We investigated the MIR properties directly measured from the spectra and discovered the following:

- 1) Local LIRGs cover a large range of MIR properties and any single LIRG cannot represent the class as a whole. LIRGs span $0.005\ \mu\text{m} < \text{EQW}_{6.2\ \mu\text{m}} < 0.78\ \mu\text{m}$ (with nondetections of the $6.2\ \mu\text{m}$ PAH reaching $\text{EQW}_{6.2\ \mu\text{m}} < 0.043\ \mu\text{m}$), $-3.51 < s_{9.7\ \mu\text{m}} < 0.052$ (with 23% of LIRGs showing silicate emission), and $2.00 < F_{\nu}[30\ \mu\text{m}]/F_{\nu}[15\ \mu\text{m}] < 35.40$. However, the majority (63%) of LIRGs have $\text{EQW}_{6.2\ \mu\text{m}} > 0.4$, $s_{9.7\ \mu\text{m}} > -1.0$, and MIR slopes in the range of $4 < F_{\nu}[30\ \mu\text{m}]/F_{\nu}[15\ \mu\text{m}] < 10$.
- 2) The GOALS ULIRGs span a narrower range of MIR properties than those covered by the LIRGs. When compared to LIRGs, the ULIRGs ($L_{\text{IR}} > 10^{12} L_{\odot}$) have a steeper median slope ($F_{\nu}[30\ \mu\text{m}]/F_{\nu}[15\ \mu\text{m}] = 12.54$ for the ULIRGs compared to $F_{\nu}[30\ \mu\text{m}]/F_{\nu}[15\ \mu\text{m}] = 7.11$ for the LIRGs), a lower mean equivalent width ($\text{EQW}_{6.2\ \mu\text{m}} = 0.30\ \mu\text{m}$ versus $\text{EQW}_{6.2\ \mu\text{m}} = 0.55\ \mu\text{m}$),

and deeper average silicate absorption ($s_{9.7\mu m} = -1.05$ versus $s_{9.7\mu m} = -0.25$).

3) There is a general trend among the U/LIRGs for both silicate depth and MIR slope to increase with increasing L_{IR} . As L_{IR} increases, the temperature may rise as a consequence of the nuclei becoming more obscured and compact. As the dust temperature increases, the rising portion of the blackbody emission spectrum shifts to shorter wavelengths, and warmer sources have increasingly more flux at $30\mu m$, and thus steeper MIR slopes. The sources that depart from these correlations, in both cases, have very low PAH equivalent width ($EQW_{6.2\mu m} < 0.1\mu m$) consistent with their MIR emission being dominated by an AGN.

4) Although less numerous (only 18% of the sample), LIRGs with the largest contributions from AGN (those with $EQW_{6.2\mu m} < 0.27\mu m$) cover a wider range of MIR slopes and silicate strengths than those sources of higher equivalent width that make up the majority of the sample. The sources with extremely low PAH equivalent widths ($EQW_{6.2\mu m} < 0.1\mu m$) separate into two distinct types: relatively unobscured sources with a very hot dust component (and thus very shallow MIR slopes) and heavily dust obscured nuclei with a steep temperature gradient. For the AGN-dominated LIRGs with low apparent obscuration, an upper limit to the MIR slope can be set at $F_{\nu}[30\mu m]/F_{\nu}[15\mu m] \sim 4$. The most obscured nuclei, however, have steeper MIR slopes due to most of their warm dust emission being hidden behind a large amount of cooler dust.

suggesting 5) The LIRGs most likely harboring buried AGN (the obscured nuclei with $s_{9.7\mu m} < -1.75$) all have $EQW_{6.2\mu m} < 0.2\mu m$ and lack any extended component to their MIR emission at $24\mu m$. Extreme levels of dust obscuration may simply be blocking PAH emission, or the higher densities in these nuclei may create an environment where PAH dust grains are not present or the conditions are not appropriate for exciting them (i.e. lacking in photodissociation regions). Their compact nature suggests that their obscuring (cool) dust is associated with the outer regions of the starburst and not simply a mea-

sure of the dust along the line of sight through a large, dusty disk.

6) U/LIRGs in the late to final stages of a merger have, on average, steeper MIR slopes and higher levels of dust obscuration. As merging galaxies coalesce and gas & dust is funneled towards the center, the nuclei become more compact and more obscured. As a result, the dust temperature increases leading also to a steeper MIR slope. A marked decline is seen for the fraction of high EQW (star formation dominated) sources as the merger progresses. The decline is accompanied by an increase in the fraction of composite sources while the fraction of sources where an AGN dominates the MIR emission remains low.

7) Despite their dusty and starburst nature, the average nearby LIRG spectrum does not resemble the average composite (starburst + AGN) MIR spectrum from submillimeter galaxies at $z \sim 2$. Both the average LIRG and ULIRG spectra are more absorbed at $9.7\mu m$ and the average LIRG has more PAH emission. However, once the AGN contributions are removed from the average LIRG and from the average SMG spectra, the PAH emission and level of silicate absorption of the average spectrum for starburst-dominated SMGs (i.e. those without AGN spectral signatures; Menéndez-Delmestre et al. 2009) are fit well by the average starburst-dominated local LIRG.

The Spitzer Space Telescope is operated by the Jet Propulsion Laboratory, California Institute of Technology, under NASA contract 1407. This research has made use of the NASA/IPAC Extragalactic Database (NED) which is operated by the Jet Propulsion Laboratory, California Institute of Technology, under contract with the National Aeronautics and Space Administration. This research has made use of the NASA/IPAC Infrared Science Archive, which is operated by the Jet Propulsion Laboratory, California Institute of Technology, under contract with the National Aeronautics Space Administration. We would like to thank M. Cluver for many helpful discussions and K. Menéndez-Delmestre for sharing her average SMG spectra.

REFERENCES

- Armus, L., Charmandaris, V., Bernard-Salas, J., et al. 2007, *ApJ*, 656, 148
- Armus, L., Mazzarella, J. M., Evans, A. S., et al. 2009, *PASP*, 121, 559
- Bernard-Salas, J., Spoon, H. W. W., Charmandaris, V., et al. 2009, *ApJS*, 184, 230
- Blain, A. W., Smail, I., Ivison, R. J., Kneib, J.-P., & Frayer, D. T. 2002, *Phys. Rep.*, 369, 111
- Brandl, B. R., Bernard-Salas, J., Spoon, H. W. W., et al. 2006, *ApJ*, 653, 1129
- Caputi, K. I., Lagache, G., Yan, L., et al. 2007, *ApJ*, 660, 97
- Dasyra, K. M., Yan, L., Helou, G., et al. 2008, *ApJ*, 680, 232
- Desai, V., Armus, L., Spoon, H. W. W., et al. 2007, *ApJ*, 669, 810
- Díaz-Santos, T., Charmandaris, V., Armus, L., et al. 2010, *ApJ*, 723, 993
- . 2011, *ApJ*, 741, 32
- Evans, A. S., Solomon, P. M., Tacconi, L. J., Vavilkin, T., & Downes, D. 2006, *AJ*, 132, 2398
- Genzel, R., Lutz, D., Sturm, E., et al. 1998, *ApJ*, 498, 579
- Haan, S., Surace, J. A., Armus, L., et al. 2011, *AJ*, 141, 100
- Houck, J. R., Roellig, T. L., van Cleve, J., et al. 2004, *ApJS*, 154, 18
- Howell, J. H., Mazzarella, J. M., Chan, B. H. P., et al. 2007, *AJ*, 134, 2086
- Howell, J. H., Armus, L., Mazzarella, J. M., et al. 2010, *ApJ*, 715, 572
- Iwasawa, K., Sanders, D. B., Teng, S. H., et al. 2011, *A&A*, 529, A106
- Le Floch, E., Papovich, C., Dole, H., et al. 2005, *ApJ*, 632, 169
- Magnelli, B., Elbaz, D., Chary, R. R., et al. 2009, *A&A*, 496, 57
- Marshall, J. A., Herter, T. L., Armus, L., et al. 2007, *ApJ*, 670, 129
- Menéndez-Delmestre, K., Blain, A. W., Smail, I., et al. 2009, *ApJ*, 699, 667
- Murphy, Jr., T. W., Armus, L., Matthews, K., et al. 1996, *AJ*, 111, 1025
- O'Dowd, M. J., Schiminovich, D., Johnson, B. D., et al. 2009, *ApJ*, 705, 885
- Petric, A. O., Armus, L., Howell, J., et al. 2011, *ApJ*, 730, 28
- Rigopoulou, D., Spoon, H. W. W., Genzel, R., et al. 1999, *AJ*, 118, 2625
- Roussel, H., Helou, G., Beck, R., et al. 2003, *ApJ*, 593, 733
- Sanders, D. B., Mazzarella, J. M., Kim, D.-C., Surace, J. A., & Soifer, B. T. 2003, *AJ*, 126, 1607
- Sanders, D. B., & Mirabel, I. F. 1996, *ARA&A*, 34, 749
- Sanders, D. B., Soifer, B. T., Elias, J. H., et al. 1988, *ApJ*, 325, 74
- Smith, J. D. T., Armus, L., Dale, D. A., et al. 2007a, *PASP*, 119, 1133

- Smith, J. D. T., Draine, B. T., Dale, D. A., et al. 2007b, ApJ, 656, 770
- Spoon, H. W. W., Keane, J. V., Tielens, A. G. G. M., Lutz, D., & Moorwood, A. F. M. 2001, A&A, 365, L353
- Spoon, H. W. W., Marshall, J. A., Houck, J. R., et al. 2007, ApJ, 654, L49
- Spoon, H. W. W., Tielens, A. G. G. M., Armus, L., et al. 2006, ApJ, 638, 759
- Stierwalt, S., et al. 2013b, ApJ, in prep
- Sturm, E., Lutz, D., Tran, D., et al. 2000, A&A, 358, 481
- Veilleux, S., Rupke, D. S. N., Kim, D.-C., et al. 2009, ApJS, 182, 628
- Wu, Y., Helou, G., Armus, L., et al. 2010, ApJ, 723, 895

TABLE 1
MID-IR SPECTRAL PARAMETERS FOR THE GOALS SAMPLE

Source Name	Short-Low RA/DEC [J2000]	(PA) [°]	Long-Low RA/DEC [J2000]	(PA) [°]	$6.2\mu\text{m}$ EQW (σ) [μm]	$9.7\mu\text{m}$ (σ)	$F_{\nu}[30\mu\text{m}]/F_{\nu}[15\mu\text{m}]$ (σ)	Scale Factor	Merge Stage	MIS (HST)
NGC00023	00h09m53.4s +25d55m26.3s	(-32.8)	00h09m53.4s +25d55m26.3s	(-116.6)	0.58 (0.01)	0.18 (0.04)	6.81 (0.04)	1.49	b	
NGC00034	00h11m06.4s -12d06m28.7s	(35.3)*	00h11m06.5s -12d06m29.2s	(117.7)*	0.45 (0.02)	-0.79 (0.03)	9.94 (0.09)	1.70	d	5
Amp256	00h18m50.9s -10d22m36.6s	(-36.1)	00h18m50.9s -10d22m36.6s	(-119.8)	0.72 (0.01)	-0.26 (0.03)	6.73 (0.07)	1.22	b	3
ESO350-IG038	00h36m52.5s -33d33m17.1s	(163.1)	00h36m52.5s -33d33m17.0s	(79.4)	0.15 (0.004)	-0.34 (0.02)	4.73 (0.01)	1.15	c	
NGC0232.W	00h42m45.8s -23d33m40.7s	(-44.6)	00h42m45.8s -23d33m40.7s	(-128.3)	0.55 (0.01)	-0.38 (0.03)	7.33 (0.03)	1.21	b	
NGC0232.E	00h42m52.8s -23d33m27.5s	(-44.6)	00h42m52.8s -23d33m27.5s	(-128.3)	0.16 (0.005)	-0.26 (0.03)	3.63 (0.03)	1.16	b	
MCG+12-02-001	00h54m03.9s +73d05m06.0s	(71.1)	00h54m03.9s +73d05m05.9s	(-12.7)	0.65 (0.01)	-0.24 (0.02)	7.19 (0.04)	1.08	c	3
NGC0317B	00h57m40.4s +43d47m32.1s	(-29.6)	00h57m40.4s +43d47m32.1s	(-113.4)	0.57 (0.01)	-0.86 (0.05)	8.23 (0.09)	1.15	a	
IC1623B	01h07m47.6s -17d30m25.4s	(25.4)*	01h07m47.3s -17d30m28.4s	(19.1)*	0.30 (0.004)	-0.98 (0.02)	7.71 (0.01)	1.73	c	3
MCG-03-04-014	01h10m09.0s -16d51m09.6s	(150.7)	01h10m08.9s -16d51m10.6s	(-126.8)	0.67 (0.01)	-0.04 (0.02)	6.98 (0.09)	1.16	N	0
ESO244-G012	01h18m08.3s -44d27m43.5s	(-79.0)	01h18m08.3s -44d27m43.6s	(-162.7)	0.66 (0.01)	-0.32 (0.13)	7.39 (0.06)	1.19	b	
CGCG436-030	01h20m02.6s +14d21m42.7s	(-27.1)	01h20m02.6s +14d21m42.7s	(-110.9)	0.35 (0.01)	-1.10 (0.10)	8.94 (0.09)	1.10	b	2
ESO353-G020	01h34m51.2s -36d08m14.5s	(-58.4)	01h34m51.2s -36d08m14.5s	(-142.1)	0.54 (0.01)	-0.58 (0.04)	7.26 (0.10)	1.42	N	
RR032.N	01h36m23.4s -37d19m18.0s	(-59.0)	01h36m23.4s -37d19m18.1s	(-142.7)	0.52 (0.01)	0.09 (0.03)	6.19 (0.10)	1.28	a	
RR032.S	01h36m24.1s -37d20m25.9s	(-58.9)	01h36m24.1s -37d20m25.9s	(-142.7)	0.70 (0.01)	-0.38 (0.04)	6.74 (0.09)	1.14	a	
IRAS F01364-1042	01h38m52.9s -10d27m11.2s	(149.2)	01h38m52.8s -10d27m12.0s	(-110.8)	0.39 (0.01)	-1.27 (0.08)	32.72 (1.04)	1.41	d	5
II Zw 035	—	—	01h44m30.5s +17d06m08.7s	(-109.1)	—	—	23.52 (0.24)	—	a	3
NGC0695	01h51m14.2s +22d34m56.4s	(-23.5)	01h51m14.3s +22d34m55.4s	(-107.3)	0.65 (0.01)	0.31 (0.02)	6.17 (0.09)	1.86	N	
UGC01385	01h54m53.8s +36d55m04.0s	(-22.0)	01h54m53.8s +36d55m04.1s	(-105.7)	0.64 (0.01)	-0.00 (0.11)	6.76 (0.08)	1.12	a	
NGC0838.W	02h09m24.7s -10d08m09.6s	(162.7)	02h09m24.7s -10d08m09.5s	(78.9)	0.45 (0.01)	0.27 (0.03)	4.76 (0.10)	1.63	a	
NGC0838.E	02h09m38.7s -10d08m47.5s	(162.6)	02h09m38.7s -10d08m47.5s	(78.9)	0.74 (0.01)	0.23 (0.03)	7.59 (0.06)	2.00	a	
NGC0838.S	02h09m42.8s -10d11m02.3s	(162.6)	02h09m42.8s -10d11m02.3s	(78.9)	0.50 (0.01)	-0.83 (0.03)	6.72 (0.04)	1.18	a	
NGC0828	02h10m09.5s +39d11m24.6s	(-19.3)	02h10m09.5s +39d11m24.7s	(-103.0)	0.61 (0.01)	-0.09 (0.03)	5.04 (0.05)	1.64	d	
IC0214	02h14m05.5s +05d10m25.4s	(-26.2)	02h14m05.4s +05d10m25.4s	(-110.0)	0.64 (0.01)	-0.05 (0.02)	6.51 (0.17)	1.34	d	
NGC0877.S	02h17m53.2s +14d31m18.1s	(-24.5)	02h17m53.2s +14d31m18.2s	(-108.3)	0.46 (0.01)	-1.16 (0.10)	7.11 (0.17)	1.36	a	
NGC0877.N	02h17m59.7s +14d32m38.0s	(-24.5)	02h17m59.6s +14d32m38.0s	(-108.3)	0.35 (0.03)	0.16 (0.03)	6.14 (0.14)	2.10	a	
MCG+05-06-036.S	02h23m19.0s +32d11m18.1s	(155.4)	02h23m19.0s +32d11m18.2s	(71.7)	0.54 (0.01)	0.19 (0.03)	6.12 (0.22)	1.46	a	2
MCG+05-06-036.N	02h23m22.0s +32d11m48.4s	(155.4)	02h23m22.0s +32d11m48.5s	(71.7)	0.48 (0.01)	-0.25 (0.02)	6.23 (0.07)	1.29	a	
UGC01845	02h24m08.0s +47d58m11.8s	(-31.2)	02h24m08.0s +47d58m11.9s	(-115.0)	0.58 (0.01)	-0.40 (0.03)	7.71 (0.09)	1.18	N	2
NGC09958	02h30m42.9s -02d45m20.4s	(-27.6)	02h30m42.9s -02d45m20.4s	(-111.3)	0.29 (0.01)	0.00 (0.08)	4.96 (0.15)	1.77	N	

Source Name	Short-Low RA/DEC [J2000]	(PA) [$^{\circ}$]	Long-Low RA/DEC [J2000]	(PA) [$^{\circ}$]	6.2 μ m EQW(σ) [μ m]	$s_{9.7\mu m}(\sigma)$	$F_{\nu}[30\mu m]/F_{\nu}[15\mu m](\sigma)$	Scale Factor	Merger Stage	MS (HST)
NGC0992	02h37m25.5s +21d06m04.4s	(-21.8)	02h37m25.5s +21d06m04.4s	(-105.5)	0.72 (0.01)	0.05 (0.04)	6.41 (0.09)	1.28	c	
UGC02238	02h46m17.5s +13d05m44.3s	(-24.7)	02h46m17.5s +13d05m44.9s	(-108.2)	0.63 (0.01)	-0.37 (0.04)	5.66 (0.07)	1.14	d	
IRASF02437+2122	02h46m39.1s +21d35m10.1s	(-22.3)	02h46m39.1s +21d35m10.3s	(-104.0)	0.16 (0.01)	-1.25 (0.06)	8.81 (0.16)	1.06	c	
UGC02369	02h54m01.8s +14d58m15.4s	(-22.9)	02h54m01.8s +14d58m15.5s	(-106.7)	0.57 (0.01)	-0.11 (0.07)	6.48 (0.03)	1.30	b	3
UGC02608_N	03h15m01.5s +42d02m08.5s	(-21.8)	03h15m01.5s +42d02m08.6s	(-105.6)	0.20 (0.003)	-0.22 (0.02)	5.04 (0.02)	1.15	N	
UGC02608_S	03h15m14.6s +41d58m49.9s	(-21.8)	03h15m14.6s +41d58m49.9s	(-105.5)	0.25 (0.14)	0.52 (0.32)	4.59 (1.60)	1.72	N	
NGC1275	03h19m48.2s +41d30m41.9s	(157.6)	03h19m48.2s +41d30m41.7s	(73.8)	0.02 (0.003)	0.26 (0.02)	2.73 (0.01)	1.01	N	
IRASF03217+4022	03h25m05.4s +40d33m32.3s	(-22.2)	03h25m05.4s +40d33m32.3s	(-105.9)	0.55 (0.01)	-0.47 (0.03)	8.34 (0.07)	1.17	d	
NGC1365	03h33m36.4s -36d08m26.0s	(-51.0)	03h33m36.4s -36d08m25.5s	(74.4)	0.13 (0.002)	0.10 (0.05)	5.65 (0.03)	1.67	N	
IRASF03359+1523	—	—	03h38m47.1s -15d32m53.2s	(-102.3)	—	—	12.45 (0.16)	—	d	
CGCG465-012_N	03h54m07.8s +15d59m24.1s	(-17.6)	03h54m07.8s +15d59m24.2s	(-101.3)	0.67 (0.02)	0.43 (0.03)	4.33 (0.16)	1.83	a	
CGCG465-012_S	03h54m16.1s +15d55m43.2s	(-17.6)	03h54m16.1s +15d55m43.3s	(-101.3)	0.60 (0.01)	-0.02 (0.03)	6.64 (0.66)	1.65	c	
IRAS03582+6012_W	04h02m32.0s +60d20m38.3s	(-12.6)	04h02m32.0s +60d20m38.3s	(-96.3)	0.64 (0.01)	0.08 (0.04)	8.80 (0.08)	—	c	
IRAS03582+6012_E	04h02m33.0s +60d20m41.8s	(-12.6)	04h02m33.0s +60d20m41.8s	(-96.3)	0.01 (0.003)	-3.04 (0.03)	6.39 (0.02)	—	c	
UGC02982	04h12m22.6s +05d32m50.5s	(-15.8)	04h12m22.6s +05d32m50.5s	(-99.6)	0.68 (0.01)	0.18 (0.03)	5.11 (0.06)	2.02	d	
ESO420-G013	04h13m49.7s -32d00m25.5s	(-49.4)	04h13m49.7s -32d00m25.5s	(-133.2)	0.30 (0.003)	-0.27 (0.03)	5.43 (0.04)	1.21	N	
NGC1572	04h22m42.8s -40d36m03.6s	(-131.6)	04h22m42.8s -40d36m03.6s	(144.7)	0.46 (0.01)	-0.16 (0.03)	6.76 (0.08)	1.20	N	
IRAS04271+3849	04h30m33.1s +38d55m48.0s	(-10.8)	04h30m33.1s +38d55m48.0s	(-94.5)	0.61 (0.01)	-0.29 (0.04)	7.85 (0.12)	1.25	d	
NGC1614	04h33m59.8s -08d34m43.1s	(-26.7)	04h33m59.8s -08d34m40.8s	(-110.4)	0.61 (0.01)	-0.41 (0.02)	4.81 (0.01)	1.40	d	5
UGC03094	04h35m33.9s +19d10m18.3s	(167.0)	04h35m33.8s +19d10m17.5s	(-97.5)	0.43 (0.005)	-0.32 (0.02)	5.05 (0.06)	1.16	N	
ESO203-IG001	04h46m49.3s -48d33m30.1s	(-106.3)	04h46m49.3s -48d33m30.1s	(170.0)	0.03 (0.01)	-3.20 (0.17)	15.05 (0.33)	0.98	d	3
MCG-05-12-006	04h52m05.0s -32d59m27.1s	(-141.0)	04h52m05.0s -32d59m27.0s	(135.3)	0.53 (0.01)	-0.02 (0.03)	7.25 (0.07)	1.11	N	
NGC1797	05h07m44.8s -08d01m08.7s	(-18.8)	05h07m44.8s -08d01m08.7s	(-102.5)	0.62 (0.01)	-0.20 (0.03)	7.72 (0.08)	1.30	a	
CGCG468-002_W	05h08m19.7s +17d21m47.5s	(173.1)	05h08m19.7s +17d21m47.5s	(89.3)	0.12 (0.005)	-0.01 (0.03)	3.75 (0.05)	1.04	b	
CGCG468-002_E	05h08m21.2s +17d22m07.7s	(173.1)	05h08m21.2s +17d22m07.7s	(89.3)	0.54 (0.01)	-0.95 (0.04)	10.38 (0.19)	1.03	b	
IRAS05083+2441_S	05h11m25.9s +24d45m18.0s	(170.4)	05h11m25.9s +24d45m18.0s	(86.6)	0.72 (0.01)	-0.16 (0.04)	7.99 (0.11)	1.17	N	
VIIZw031	05h16m46.4s +79d40m12.7s	(155.0)	05h16m46.3s +79d40m12.7s	(71.3)	0.64 (0.01)	-0.22 (0.04)	7.37 (0.11)	1.27	N	0
IRAS05129+5128	05h16m56.0s +51d31m57.3s	(2.3)	05h16m56.0s +51d31m57.3s	(-81.5)	0.54 (0.01)	-0.61 (0.04)	8.75 (0.11)	1.27	d	
IRASF05189-2524	05h21m01.3s -25d21m45.6s	(-2.5)	05h21m01.4s -25d21m46.1s	(-86.2)	0.03 (0.002)	-0.29 (0.02)	5.04 (0.01)	0.98	d	
IRASF05187-1017	05h21m06.5s -10d14m46.8s	(-13.7)	05h21m06.5s -10d14m46.2s	(-108.7)	0.53 (0.03)	-0.64 (0.14)	14.90 (0.51)	1.06	N	

Source Name	Short-Low RA/DEC [J2000]	(PA) [°]	Long-Low RA/DEC [J2000]	(PA) [°]	6.2 μ m EQW(σ) [μ m]	$s_9\text{-}\tau_{9\mu\text{m}}$ (σ)	$F_{\nu}[30\mu\text{m}]/F_{\nu}[15\mu\text{m}]$ (σ)	Scale Factor	Merger Stage	MS (HST)
IRAS05223+1908	05h25m16.7s +19d10m48.0s	(-10.1)	05h25m16.7s +19d10m48.0s	(-93.8)	<0.01 (—)	0.12 (0.02)	2.00 (0.01)	0.99	N	
MCG+08-11-002	05h40m43.7s +49d41m41.3s	(169.6)	05h40m43.7s +49d41m41.3s	(85.9)	0.56 (0.01)	-0.89 (0.03)	9.47 (0.08)	1.22	d	
NGC1961	05h42m04.7s +69d22m43.1s	(162.9)	05h42m04.7s +69d22m43.2s	(79.2)	0.24 (0.01)	0.03 (0.09)	4.18 (0.05)	1.93	d	
UGC033351	05h45m48.2s +58d42m03.1s	(155.1)	05h45m48.1s +58d42m03.2s	(71.4)	0.53 (0.01)	-0.68 (0.04)	6.88 (0.10)	1.07	a	
IRAS05442+1732	05h47m11.2s +17d33m46.5s	(-9.3)	05h47m11.2s +17d33m46.6s	(-93.0)	0.66 (0.01)	-0.38 (0.02)	7.52 (0.03)	1.16	a	
IRASF06076-2139	06h09m45.8s -21d40m23.9s	(166.3)	06h09m45.8s -21d40m23.8s	(110.0)	0.33 (0.02)	-1.39 (0.09)	7.98 (0.10)	—	c	
UGC03410_W	06h13m58.8s +80d28m35.2s	(154.7)	06h13m58.8s +80d28m35.2s	(70.8)	0.62 (0.01)	0.15 (0.04)	3.38 (0.06)	1.60	a	
UGC03410_E	06h14m30.5s +80d26m59.9s	(154.6)	06h14m30.5s +80d26m59.9s	(71.0)	0.63 (0.01)	0.14 (0.05)	5.19 (0.03)	1.79	a	
NGC2146	06h18m37.5s +78d21m24.3s	(17.7)	06h18m37.7s +78d21m25.8s	(-62.4)	0.67 (0.01)	-0.43 (0.02)	9.96 (0.01)	2.43	d	
ESO255-IG007_W	06h27m21.7s -47d10m36.5s	(-128.8)	06h27m21.7s -47d10m36.4s	(147.4)	0.62 (0.01)	-0.26 (0.02)	8.31 (0.03)	—	b	3
ESO255-IG007_E	06h27m22.5s -47d10m47.6s	(-128.8)	06h27m22.5s -47d10m47.5s	(147.4)	0.65 (0.02)	0.26 (0.02)	8.05 (0.04)	—	b	3
ESO255-IG007_S	06h27m23.1s -47d11m02.9s	(-128.8)	06h27m23.1s -47d11m02.9s	(147.4)	0.69 (0.02)	-0.10 (0.02)	7.27 (0.04)	—	b	3
ESO557-G002_S	06h31m45.7s -17d38m44.8s	(-167.6)	06h31m45.7s -17d38m44.7s	(108.7)	0.70 (0.07)	0.34 (0.06)	6.42 (0.64)	1.09	a	
ESO557-G002_N	06h31m47.2s -17d37m16.5s	(-167.6)	06h31m47.2s -17d37m16.4s	(108.7)	0.60 (0.01)	-0.73 (0.04)	12.18 (0.09)	1.04	a	
UGC003608	06h57m34.4s +46d24m10.7s	(174.4)	06h57m34.4s +46d24m10.7s	(90.6)	0.53 (0.01)	-0.32 (0.03)	7.40 (0.07)	1.13	b	
IRASF06592-6313	06h59m40.3s -63d17m52.5s	(-164.8)	06h59m40.3s -63d17m52.5s	(111.5)	0.48 (0.01)	-0.31 (0.04)	6.98 (0.08)	1.10	N	
AM0702-601_N	07h03m24.1s -60d15m21.8s	(-163.8)	07h03m24.1s -60d15m21.8s	(112.4)	0.04 (0.002)	-0.10 (0.02)	3.11 (0.01)	1.24	a	1
AM0702-601_S	07h03m28.5s -60d16m43.6s	(-163.8)	07h03m28.5s -60d16m43.6s	(112.4)	0.68 (0.01)	-0.05 (0.03)	7.21 (0.72)	1.37	a	
NGC2342	07h09m18.1s +20d38m09.5s	(2.6)	07h09m18.1s +20d38m09.9s	(99.4)	0.67 (0.01)	-0.06 (0.03)	8.07 (0.11)	1.28	a	
NGC2369	07h16m37.9s -62d20m36.4s	(50.9)*	07h16m37.8s -62d20m34.2s	(43.2)*	0.48 (0.01)	-0.60 (0.02)	5.88 (0.02)	1.65	N	
IRAS07251-0248	07h27m37.6s -02d54m54.2s	(-170.4)	07h27m37.6s -02d54m54.2s	(105.9)	0.09 (0.01)	-2.35 (0.14)	13.38 (0.12)	1.10	d	
NGC2388	07h28m53.4s +33d49m08.9s	(-173.9)	07h35m41.5s +11d36m42.0s	(102.3)	0.53 (0.005)	0.07 (0.06)	—	—	a	
MCG+02-20-003_S	07h35m41.5s +11d36m42.0s	(-173.9)	07h35m41.5s +11d36m42.0s	(102.3)	0.58 (0.05)	0.47 (0.18)	4.62 (0.66)	1.74	a	
MCG+02-20-003_N	07h35m43.5s +11d42m34.7s	(-173.9)	07h35m43.4s +11d42m34.7s	(102.3)	0.17 (0.003)	-0.49 (0.04)	10.08 (0.14)	1.26	a	
IRAS08355-4944	08h37m01.8s -49d54m30.3s	(-155.8)	08h37m01.8s -49d54m30.2s	(120.5)	0.19 (0.003)	-0.32 (0.02)	6.59 (0.04)	1.16	d	3
IRASF08339+6517	—	—	08h38m23.2s +65d07m14.5s	(109.0)	—	—	7.37 (0.05)	—	N	
NGC2623	08h38m24.1s +25d45m17.4s	(11.9)	08h38m24.1s +25d45m17.2s	(-71.8)	0.27 (0.01)	-1.12 (0.05)	14.66 (0.13)	1.05	d	5
ESO432-IG006_W	08h44m27.2s -31d41m50.9s	(-155.6)	08h44m27.2s -31d41m50.8s	(120.7)	0.64 (0.01)	0.02 (0.04)	6.23 (0.11)	1.29	b	
ESO432-IG006_E	08h44m28.9s -31d41m30.4s	(-155.6)	08h44m28.9s -31d41m30.3s	(120.7)	0.41 (0.01)	-0.01 (0.07)	6.91 (0.14)	1.05	b	
ESO60-IG016	08h52m31.8s -69d01m55.8s	(-84.5)	08h52m31.8s -69d01m55.7s	(-168.2)	0.11 (0.004)	-1.76 (0.04)	7.71 (0.04)	1.09	b	3

Source Name	Short-Low RA/DEC [J2000]	(PA) [°]	Long-Low RA/DEC [J2000]	(PA) [°]	6.2 μ m EQW [μm]	$s_{9.7\mu m}(\sigma)$	$F_{\nu}[30\mu m]/F_{\nu}[15\mu m](\sigma)$	Scale Factor	Merger Stage	MS (HST)
IRASF08572+3915	09h00m25.4s +39d03m54.6s	(19.0)	09h00m25.4s +39d03m55.1s	(-64.7)	<0.03 (—)	-3.58 (0.04)	5.24 (0.01)	1.01	d	3
IRAS09022-3615	09h04m12.7s -36d27m01.6s	(23.2)	09h04m12.7s -36d27m01.7s	(-60.5)	0.14 (0.004)	-0.88 (0.03)	7.97 (0.05)	1.05	d	
IRASF09111-1007_W	09h13m36.5s -10d19m30.0s	(-160.9)	09h13m36.5s -10d19m29.9s	(115.4)	0.47 (0.02)	-0.73 (0.10)	12.54 (0.39)	1.13	b	
IRASF09111-1007_E	09h13m38.9s -10d19m19.9s	(-160.9)	09h13m38.9s -10d19m19.9s	(115.4)	0.52 (0.03)	-0.15 (0.07)	5.91 (0.26)	1.30	b	
UGC04881_W	09h15m54.7s +44d19m50.7s	(-161.0)	09h15m54.7s +44d19m50.7s	(115.3)	0.61 (0.01)	-0.27 (0.04)	9.17 (0.31)	1.10	c	
UGC04881_E	09h15m55.5s +44d19m57.2s	(-161.0)	09h15m55.5s +44d19m57.3s	(115.3)	0.40 (0.01)	-0.81 (0.04)	10.22 (0.17)	1.01	c	
UGC05101	09h35m51.6s +61d21m11.7s	(47.4)	09h35m51.7s +61d21m12.0s	(-36.4)	0.13 (0.005)	-0.78 (0.05)	7.69 (0.05)	0.99	d	
MCG+08-18-013	—	—	09h36m37.2s +48d28m27.9s	(119.2)	—	—	7.48 (0.05)	—	a	
Arp303_S	09h46m20.3s +03d02m44.3s	(-163.3)	09h46m20.3s +03d02m44.4s	(112.9)	0.60 (0.02)	0.06 (0.04)	6.06 (0.11)	2.55	a	
Arp303_N	09h46m21.1s +03d04m15.9s	(-163.3)	09h46m21.1s +03d04m16.0s	(112.9)	0.57 (0.06)	0.08 (0.09)	4.56 (0.10)	1.58	a	
NGC3110	10h04m02.0s -06d28m29.5s	(161.6)*	10h04m02.2s -06d28m31.9s	(65.7)*	0.64 (0.01)	0.19 (0.03)	5.91 (0.04)	2.10	a	
ESO374-IG032	10h06m04.7s -33d53m06.3s	(-128.3)	10h06m04.7s -33d53m06.2s	(148.0)	0.03 (0.002)	-2.74 (0.04)	9.36 (0.03)	1.13	d	
IRASF10173+0828	10h20m00.2s +08d13m33.8s	(-162.9)	10h20m00.2s +08d13m33.6s	(113.3)	0.35 (0.04)	-1.20 (0.12)	35.40 (1.38)	1.07	a	
NGC3221	10h22m20.3s +21d34m22.1s	(-162.9)	10h22m20.3s +21d34m22.1s	(113.3)	0.75 (0.01)	-0.12 (0.04)	5.94 (0.05)	1.44	N	
NGC3256	10h27m51.2s -43d54m13.8s	(-5.5)	10h27m51.3s -43d54m13.9s	(-57.4)	0.61 (0.01)	-0.28 (0.02)	8.16 (0.04)	1.33	d	5
ESO264-G036	10h43m07.5s -46d12m44.3s	(-111.2)	10h43m07.5s -46d12m44.3s	(165.0)	0.44 (0.01)	-0.04 (0.02)	5.49 (0.03)	1.87	N	
ESO264-G057	10h59m01.8s -43d26m25.8s	(-137.5)	10h59m01.8s -43d26m25.8s	(138.8)	0.60 (0.01)	-0.19 (0.04)	7.46 (0.10)	1.34	d	
IRASF10565+2448	10h59m18.1s +24d32m34.9s	(25.3)	10h59m18.1s +24d32m35.4s	(-58.4)	0.51 (0.01)	-0.75 (0.04)	9.51 (0.07)	1.08	d	2
MCG+07-23-019	11h03m54.0s +40d51m00.7s	(-159.7)	11h03m54.0s +40d51m00.7s	(116.6)	0.64 (0.01)	-0.55 (0.03)	12.40 (1.24)	1.14	d	
CGCG01-076	11h21m12.2s -02d59m02.4s	(164.4)*	11h21m12.3s -02d59m03.0s	(157.9)*	0.32 (0.02)	-0.42 (0.03)	4.35 (0.05)	1.30	a	
IRASF11231+1456	11h25m45.1s +14d40m35.8s	(-166.8)	11h25m45.1s +14d40m36.4s	(117.0)	0.60 (0.01)	-0.22 (0.03)	8.90 (0.20)	0.93	a	1
ESO319-G022	11h27m54.1s -41d36m52.4s	(-126.3)	11h27m54.1s -41d36m52.4s	(150.0)	0.42 (0.02)	-0.30 (0.05)	10.81 (0.17)	1.11	d	
NGC3690_W	11h28m31.1s +58d33m41.6s	(108.8)*	11h28m31.1s +58d33m43.6s	(44.3)*	0.12 (0.002)	-0.77 (0.02)	4.48 (0.00)	—	c	3
NGC3690_E	11h28m33.8s +58d33m47.0s	(51.5)*	11h28m33.7s +58d33m48.3s	(44.3)*	0.38 (0.003)	-1.65 (0.02)	12.12 (0.01)	1.44	c	3
ESO320-G030	11h53m11.6s -39d07m47.3s	(166.3)*	11h53m11.6s -39d07m45.6s	(158.2)*	0.58 (0.01)	-0.22 (0.02)	13.24 (0.05)	1.44	N	
ESO440-IG058_N	12h06m51.7s -31d56m46.4s	(-152.0)	12h06m51.7s -31d56m46.3s	(124.3)	0.56 (0.02)	0.37 (0.04)	9.80 (0.98)	—	b	
ESO440-IG058_S	12h06m51.9s -31d56m59.2s	(-152.0)	12h06m51.9s -31d56m59.1s	(124.3)	0.66 (0.01)	-0.45 (0.03)	7.56 (0.06)	1.21	b	
IRASF12112+0305	12h13m46.0s +02d48m40.8s	(-161.5)	12h13m46.0s +02d48m40.6s	(114.8)	0.30 (0.03)	-1.24 (0.14)	16.65 (0.34)	1.13	d	4
ESO267-G030_W	12h13m52.3s -47d16m25.9s	(-132.3)	12h13m52.3s -47d16m25.8s	(144.0)	0.68 (0.01)	-0.08 (0.04)	7.39 (0.10)	1.15	a	
NGC4194	12h14m09.6s +54d31m34.3s	(179.7)	12h14m09.5s +54d31m33.8s	(96.0)	0.55 (0.005)	-0.29 (0.02)	7.65 (0.05)	1.37	d	

Source	Short-Low RA/DEC [J2000]	(PA) [$^{\circ}$]	Long-Low RA/DEC [J2000]	(PA) [$^{\circ}$]	$6.2\mu\text{m}$ EQW(σ) [μm]	$s_{9.7\mu\text{m}}$ (σ)	$F_{\nu}[30\mu\text{m}]/F_{\nu}[15\mu\text{m}](\sigma)$	Scale Factor	Merger Stage	MIS (HST)
ESO267-G030_E	12h14m12.8s -47d13m43.0s	(-132.4)	12h14m12.8s -47d13m42.9s	(143.9)	0.50 (0.01)	-0.01 (0.03)	4.86 (0.06)	1.61	a	
IRAS12116-5615	12h14m22.1s -56d32m32.9s	(-132.4)	12h14m22.1s -56d32m32.8s	(143.9)	0.36 (0.01)	-0.85 (0.03)	7.93 (0.07)	1.11	N	0
IRAS12222-4-0624	12h25m03.9s -06d40m52.2s	(17.5)	12h25m03.9s -06d40m52.1s	(-66.3)	0.07 (0.02)	-2.12 (0.15)	28.34 (1.46)	0.95	N	
NGC4418	12h26m54.6s -00d52m40.0s	(18.9)	12h26m54.6s -00d52m40.1s	(-64.8)	<0.02 (—)	-3.51 (0.09)	7.83 (0.01)	1.04	N	
UGC08058	12h56m14.3s +56d52m25.4s	(80.3)	12h56m14.4s +56d52m24.7s	(-3.4)	0.01 (0.001)	-0.48 (0.02)	3.67 (0.01)	1.02	d	
NGC4922	13h01m25.3s +29d18m50.0s	(-164.9)	—	—	0.16 (0.003)	-0.60 (0.24)	—	—	c	
CGCG043-099	13h01m50.3s +04d20m00.1s	(-160.9)	13h01m50.3s +04d20m00.2s	(111.4)	0.55 (0.01)	-0.81 (0.03)	9.12 (0.17)	1.14	d	
MCG-02-33-098_W	13h02m19.7s -15d46m04.0s	(-160.9)	13h02m19.7s -15d46m03.9s	(115.3)	0.55 (0.01)	-0.04 (0.03)	5.77 (0.07)	1.15	b	
MCG-02-33-098_E	13h02m20.4s -15d45m59.4s	(-160.9)	13h02m20.4s -15d45m59.3s	(115.3)	0.70 (0.02)	0.04 (0.05)	8.47 (0.21)	1.29	b	
ESO507-G070	13h02m52.4s -23d55m18.3s	(-153.1)	13h02m52.4s -23d55m18.2s	(123.2)	0.56 (0.01)	-1.24 (0.10)	13.58 (0.19)	1.10	d	
IRAS13052-5711	13h08m18.7s -57d27m29.9s	(-144.6)	13h08m18.7s -57d27m29.9s	(131.7)	0.61 (0.01)	-0.51 (0.03)	12.09 (0.21)	1.12	a	
IC0860	13h15m03.5s +24d37m08.0s	(-177.8)	13h15m03.5s +24d37m08.1s	(98.4)	0.43 (0.01)	-0.98 (0.11)	33.15 (0.29)	1.14	N	
IRAS13120-5453	13h15m06.5s -55d09m23.6s	(-137.2)	13h15m06.5s -55d09m23.8s	(139.1)	0.45 (0.01)	-0.91 (0.03)	12.54 (0.07)	1.26	b	5
VY250a_W	13h15m30.7s +62d07m45.7s	(-137.5)	13h15m30.7s +62d07m45.7s	(138.8)	0.76 (0.03)	-0.23 (0.11)	8.09 (0.33)	1.35	b	2
VY250a_E	13h15m35.0s +62d07m29.1s	(-137.5)	13h15m35.0s +62d07m29.1s	(138.8)	0.63 (0.01)	-0.67 (0.03)	7.65 (0.05)	1.03	b	2
UGC08387	13h20m35.4s +34d08m22.1s	(-169.5)	13h20m35.4s +34d08m22.2s	(105.6)	0.62 (0.01)	-1.01 (0.03)	10.80 (0.10)	1.07	d	4
UGC5104	13h21m23.1s +00d20m32.6s	(-167.4)	13h21m23.2s +00d20m33.2s	(113.7)	0.51 (0.01)	-0.47 (0.04)	6.67 (0.11)	1.21	N	
MCG-03-34-064	13h22m24.5s -16d43m42.7s	(-159.5)	13h22m24.5s -16d43m42.6s	(116.8)	<0.01 (—)	-0.18 (0.02)	2.13 (0.00)	0.96	a	
NGC5135	13h25m44.1s -29d45m00.7s	(15.0)	13h25m44.2s -29d45m00.4s	(-68.7)	0.49 (0.01)	-0.24 (0.02)	5.78 (0.03)	1.53	N	
ESO173-G015	13h27m23.8s -57d29m21.7s	(-148.7)	13h27m23.8s -57d29m21.6s	(127.5)	0.53 (0.01)	-0.13 (0.08)	15.04 (0.07)	—	N	
IC4280	13h32m53.4s -24d12m25.3s	(-157.6)	13h32m53.4s -24d12m25.2s	(118.6)	0.59 (0.01)	0.13 (0.04)	5.24 (0.09)	1.56	N	
NGC5256	13h38m17.7s +48d16m32.9s	(-162.4)	13h38m17.6s +48d16m33.9s	(113.9)	0.44 (0.02)	-0.47 (0.03)	6.41 (0.03)	—	b	3
Arp240_W	13h39m53.0s +00d50m25.3s	(19.1)	13h39m53.0s +00d50m25.3s	(-64.6)	0.63 (0.01)	-0.01 (0.03)	7.18 (0.19)	1.66	b	2
Arp240_E	13h39m57.7s +00d49m51.0s	(19.1)	13h39m57.7s +00d49m51.0s	(-64.6)	0.54 (0.01)	0.12 (0.03)	6.31 (0.19)	1.69	b	
UGC08696	13h44m42.2s +55d53m13.2s	(93.5)	13h44m42.3s +55d53m12.6s	(9.8)	0.12 (0.01)	-1.37 (0.05)	12.36 (0.07)	1.06	d	4
UGC08739	13h49m13.9s +35d15m26.6s	(-169.7)	13h49m13.9s +35d15m26.6s	(106.5)	0.51 (0.01)	-0.59 (0.03)	6.74 (0.12)	2.14	N	
ESO221-IG010	13h50m56.9s -49d03m19.2s	(-153.3)	13h50m56.9s -49d03m19.1s	(123.0)	0.69 (0.01)	0.03 (0.03)	7.26 (0.08)	1.48	N	
NGC5331_S	13h52m16.2s +02d06m05.5s	(-171.0)	13h52m16.2s +02d06m05.5s	(105.2)	0.61 (0.01)	-0.43 (0.03)	7.06 (0.10)	1.19	c	3
NGC5331_N	13h52m16.5s +02d06m31.3s	(-171.0)	13h52m16.4s +02d06m31.3s	(105.2)	0.60 (0.01)	0.13 (0.03)	5.24 (0.24)	1.11	c	3
Arp84_N	13h58m33.6s +37d27m13.2s	(-178.0)	13h58m33.6s +37d27m13.2s	(98.2)	0.62 (0.01)	-0.08 (0.03)	6.84 (0.03)	1.09	c	

Source Name	Short-Low RA/DEC [J2000]	(PA) [°]	Long-Low RA/DEC [J2000]	(PA) [°]	6.2 μ m EQW(σ) [μ m]	s _{9.7μm} (σ)	F_{ν} [30 μ m]/ F_{ν} [15 μ m](σ)	Scale Factor	Merger Stage	MS (HST)
Arp84_S	13h58m37.9s +37d25m28.2s	(-178.0)	13h58m37.9s +37d25m28.2s	(98.2)	0.17 (0.02)	0.52 (0.07)	3.82 (0.24)	2.10	c	
CGCG247-020	14h19m43.3s +49d14m11.5s	(-152.2)	14h19m43.3s +49d14m11.6s	(115.2)	0.56 (0.01)	-0.20 (0.03)	7.64 (0.10)	1.13	N	
NGC5653	14h30m10.4s +31d12m56.1s	(172.7)	14h30m10.4s +31d12m56.1s	(89.0)	0.54 (0.01)	0.25 (0.03)	7.35 (0.04)	—	N	
IRASF14348-1447	14h37m38.4s -15d00m24.0s	(-167.2)	14h37m38.3s -15d00m24.6s	(109.1)	0.25 (0.01)	-1.36 (0.16)	16.76 (0.36)	1.14	d	4
IRASF14378-3651	14h40m59.0s -37d04m33.1s	(-160.3)	14h40m58.9s -37d04m33.0s	(116.0)	0.39 (0.03)	-1.14 (0.16)	15.71 (0.30)	1.08	d	6
NGC5734_N	14h45m09.0s -20d52m13.2s	(-167.1)	14h45m09.0s -20d52m13.2s	(109.1)	0.47 (0.01)	0.12 (0.03)	5.01 (0.14)	1.66	a	
NGC5734_S	14h45m11.0s -20d54m48.7s	(-167.1)	14h45m11.0s -20d54m48.5s	(109.1)	0.49 (0.01)	-0.04 (0.04)	5.07 (0.08)	2.15	a	
VV340a_S	14h57m00.3s +24d36m24.2s	(177.8)	14h57m00.3s +24d36m24.3s	(94.1)	0.58 (0.02)	0.33 (0.04)	4.82 (0.31)	1.37	b	1
VV340a_N	14h57m00.7s +24d37m05.4s	(177.8)	14h57m00.7s +24d37m05.5s	(94.1)	0.58 (0.01)	-0.63 (0.03)	6.21 (0.10)	0.82	b	1
CGCG049-057	15h13m13.1s +07d13m33.1s	(155.9)*	15h13m13.0s +07d13m35.2s	(59.8)*	0.51 (0.04)	-0.83 (0.03)	31.40 (0.39)	1.05	N	
VV705	15h18m06.4s +42d44m36.6s	(-145.5)	—	—	0.75 (0.06)	0.32 (0.06)	—	—	b	
ESO099-G004	15h24m58.0s -63d07m29.2s	(-169.3)	15h24m58.0s -63d07m29.1s	(106.9)	0.53 (0.01)	-0.78 (0.04)	7.74 (0.06)	1.04	d	3
IRASF15250+3608	15h26m59.4s +35d58m37.7s	(170.1)	15h26m59.4s +35d58m37.2s	(86.3)	0.03 (0.01)	-2.69 (0.07)	10.52 (0.03)	0.97	d	5
NGC5936	15h30m00.8s +12d59m22.3s	(-172.2)	15h30m00.8s +12d59m22.4s	(104.0)	0.62 (0.01)	-0.13 (0.03)	6.41 (0.07)	1.25	N	
Arp220	15h34m57.3s +23d30m11.7s	(178.0)	15h34m57.2s +23d30m11.1s	(94.2)	0.17 (0.004)	-2.26 (0.06)	20.38 (1.67)	1.08	d	4
NGC5990	15h46m16.4s +02d24m55.7s	(-171.3)	15h46m16.4s +02d24m55.8s	(104.9)	0.15 (0.002)	-0.11 (0.03)	4.74 (0.02)	1.22	a	
NGC6052	16h05m13.1s +20d32m35.6s	(59.0)*	16h05m12.9s +20d32m35.5s	(51.7)*	0.69 (0.03)	-0.06 (0.03)	6.63 (0.04)	3.08	c	
NGC6090	16h11m40.2s +52d27m24.9s	(26.8)	16h11m40.3s +52d27m24.7s	(-57.0)	0.73 (0.02)	-0.04 (0.03)	7.54 (0.03)	—	c	4
IRASF16164-0746	16h19m11.8s -07d54m02.7s	(-177.8)	16h19m11.8s -07d54m02.7s	(102.1)	0.61 (0.01)	-1.18 (0.07)	11.58 (0.20)	1.03	d	5
CGCG052-037	16h30m56.5s +04d04m58.5s	(16.1)	16h30m56.5s +04d04m58.8s	(101.2)	0.62 (0.01)	-0.21 (0.02)	7.07 (0.09)	1.16	N	
NGC6156	16h34m52.5s -60d37m07.5s	(-179.8)	16h34m52.5s -60d37m07.5s	(96.4)	0.37 (0.01)	0.47 (0.02)	5.89 (0.02)	1.23	N	
ESO069-IG006	16h38m11.8s -68d26m08.0s	(178.6)	16h38m11.8s -68d26m07.9s	(94.8)	0.64 (0.01)	-0.40 (0.04)	7.91 (0.10)	1.17	b	2
IRASF16399-0937	16h42m40.1s -09d43m13.5s	(-176.4)	16h42m40.1s -09d43m13.4s	(99.9)	0.43 (0.01)	-1.12 (0.04)	9.09 (0.09)	1.14	d	3
ESO453-G005_N	16h47m29.4s -29d19m06.8s	(-175.6)	16h47m29.4s -29d19m06.7s	(100.7)	0.74 (0.07)	0.47 (0.05)	5.21 (0.14)	1.51	N	
ESO453-G005_S	16h47m31.1s -29d21m21.6s	(-175.6)	16h47m31.1s -29d21m21.5s	(100.6)	0.42 (0.01)	-0.47 (0.09)	27.11 (2.71)	1.22	N	
NGC6240	16h52m58.9s +02d24m03.7s	(-177.4)	16h52m58.9s +02d24m03.0s	(98.9)	0.35 (0.01)	-0.92 (0.07)	7.72 (0.04)	1.05	d	4
IRASF16516-0948	16h54m23.9s -09d53m20.6s	(-177.9)	16h54m23.9s -09d53m20.5s	(98.4)	0.69 (0.01)	0.18 (0.03)	7.02 (0.15)	1.67	d	
NGC6286_N	16h58m24.0s +58d57m21.4s	(-117.4)	16h58m24.0s +58d57m21.9s	(116.3)	0.66 (0.02)	0.08 (0.03)	6.81 (0.07)	1.14	b	
NGC6286_S	16h58m31.3s +58d56m10.7s	(27.8)	16h58m31.7s +58d56m13.5s	(116.3)	0.59 (0.01)	-0.40 (0.03)	5.97 (0.04)	0.91	b	
IRASF17132+5313	—	—	17h14m20.2s +53d10m30.4s	(-102.2)	—	—	9.67 (0.97)	—	b	

Source Name	Short-Low			Long-Low			6.2 μ m	EQW(σ)	$s_{9.7\mu\text{m}}(\sigma)$	$F_{\nu}[30\mu\text{m}]/F_{\nu}[15\mu\text{m}](\sigma)$	Scale Factor	Merger Stage	MS (HST)
	RA/DEC	(PA)	(θ)	RA/DEC	(PA)	(θ)							
IRAS17138-1017	17h16m35.6s -10d20m37.9s	(173.8)	17h16m36.0s -10d20m41.2s	(1.2)*	0.68 (0.01)	-0.37 (0.04)	7.17 (1.51)	4.12	d	6			
IRAS17207-0014	17h23m22.0s -00d17m00.8s	(173.2)	17h23m22.0s -00d17m01.0s	(89.5)	0.31 (0.01)	-1.26 (0.07)	26.39 (0.24)	1.22	d	5			
ESO138-G027	17h26m43.4s -59d55m54.8s	(-177.1)	17h26m43.3s -59d55m55.7s	(99.1)	0.52 (0.01)	-0.35 (0.06)	8.13 (0.03)	1.14	N				
UGC11041	17h54m51.9s +34d46m34.0s	(-14.4)	17h54m51.9s +34d46m34.0s	(-98.2)	0.58 (0.01)	0.07 (0.03)	5.27 (0.04)	2.26	N				
CGCG141-034	17h56m56.6s +24d01m01.8s	(-11.9)	17h56m56.6s +24d01m01.8s	(-95.6)	0.48 (0.01)	-0.64 (0.06)	9.35 (0.16)	1.18	N				
IRAS17578-0400_W	18h00m24.3s -04d01m04.2s	(171.6)	18h00m24.3s -04d01m04.1s	(87.9)	0.62 (0.02)	0.16 (0.09)	8.56 (0.25)	2.28	b				
IRAS17578-0400_N	18h00m31.8s -04d00m53.8s	(171.6)	18h00m31.8s -04d00m53.7s	(87.9)	0.68 (0.01)	-0.67 (0.05)	21.18 (0.24)	1.45	b				
IRAS17578-0400_S	18h00m34.1s -04d01m44.3s	(171.6)	18h00m34.1s -04d01m44.2s	(87.9)	0.78 (0.01)	0.15 (0.07)	6.38 (0.21)	1.83	a				
IRAS18090+0130_W	18h11m33.4s +01d31m42.3s	(169.3)	18h11m33.4s +01d31m42.4s	(85.5)	0.52 (0.03)	-0.72 (0.10)	8.04 (0.26)	1.19	b				
IRAS18090+0130_E	18h11m38.4s +01d31m40.2s	(169.3)	18h11m38.4s +01d31m40.3s	(85.5)	0.61 (0.01)	-0.28 (0.04)	7.16 (0.06)	1.22	b				
NGC6621	18h12m55.2s +68d21m48.4s	(21.6)*	18h12m54.8s +68d21m48.7s	(5.2)*	0.56 (0.01)	-0.16 (0.02)	5.83 (0.01)	1.26	b				
IC4687	18h13m39.7s -57d43m30.5s	(13.6)*	18h13m40.2s -57d43m33.5s	(2.1)*	0.73 (0.02)	0.12 (0.02)	6.50 (0.02)	1.56	b				
CGCG142-034_W	18h16m33.8s +22d06m38.9s	(172.9)	18h16m33.8s +22d06m39.0s	(89.1)	0.48 (0.01)	-0.24 (0.03)	5.62 (0.21)	1.03	a				
CGCG142-034_E	18h16m40.7s +22d06m46.4s	(172.9)	18h16m40.7s +22d06m46.5s	(89.1)	0.51 (0.01)	-0.48 (0.03)	7.34 (0.11)	1.95	a				
IRAS18293-3413	18h32m41.1s -34d11m27.1s	(-8.8)	18h32m41.1s -34d11m27.1s	(-92.5)	0.63 (0.01)	-0.51 (0.02)	7.66 (0.05)	1.38	c				
NGC6670_W	18h33m34.3s +59d53m17.9s	(-7.3)	18h33m34.3s +59d53m17.9s	(-91.0)	0.63 (0.01)	-0.22 (0.03)	8.82 (0.11)	1.85	b				
NGC6670_E	18h33m37.8s +59d53m22.8s	(-7.3)	18h33m37.8s +59d53m22.8s	(-91.0)	0.61 (0.01)	-0.34 (0.03)	8.78 (0.10)	1.26	b				
IC4734	18h38m25.8s -57d29m25.4s	(167.4)	18h38m25.8s -57d29m25.3s	(83.7)	0.51 (0.01)	-0.60 (0.04)	8.26 (0.09)	1.35	N				
NGC6701	18h43m12.5s +60d39m11.9s	(-6.0)	18h43m12.5s +60d39m11.9s	(-83.2)	0.55 (0.01)	-0.15 (0.09)	7.10 (0.07)	1.27	N				
VV414_W	19h10m53.9s +73d24m36.1s	(0.6)	19h10m53.9s +73d24m36.1s	(-83.2)	0.64 (0.01)	0.10 (0.03)	7.24 (0.06)	1.41	c				
VV414_E	19h11m04.3s +73d25m32.6s	(0.6)	19h11m04.3s +73d25m32.6s	(-83.1)	0.29 (0.01)	-0.08 (0.02)	5.46 (0.02)	1.08	c				
ESO593-IG008	19h14m31.2s -21d19m06.4s	(-13.2)	19h14m31.2s -21d19m06.3s	(-96.9)	0.56 (0.01)	-0.59 (0.03)	8.92 (0.12)	1.38	d				
IRAS19297-0406	19h32m22.3s -04d00m00.2s	(156.3)	19h32m22.3s -04d00m00.2s	(72.6)	0.30 (0.02)	-1.05 (0.13)	15.07 (0.25)	1.16	N				
IRAS19542+1110	19h56m35.8s +11d19m05.4s	(-6.4)	19h56m35.8s +11d19m05.4s	(-90.1)	0.29 (0.02)	-0.74 (0.08)	14.53 (0.31)	1.07	N				
ESO339-G011	19h57m37.6s -37d56m08.4s	(-22.0)	19h57m37.6s -37d56m08.4s	(-105.8)	0.27 (0.01)	-0.31 (0.03)	4.64 (0.04)	1.22	N				
NGC6907	20h25m06.5s -24d48m32.6s	(-22.2)	20h25m06.5s -24d48m32.5s	(-105.9)	0.57 (0.01)	0.10 (0.03)	6.67 (0.04)	1.62	N				
MCG+04-48-002	20h28m35.1s +25d44m00.2s	(2.8)	20h28m35.1s +25d44m00.2s	(-80.9)	0.57 (0.01)	-0.47 (0.03)	5.22 (0.05)	1.73	a				
NGC6926	20h33m06.1s -02d01m38.8s	(-12.0)	20h33m06.1s -02d01m38.7s	(-95.7)	0.37 (0.01)	-0.49 (0.03)	5.07 (0.05)	1.45	d				
IRAS20351+2521	20h37m17.7s +25d31m39.1s	(3.8)	20h37m17.7s +25d31m39.1s	(-79.9)	0.57 (0.01)	-0.24 (0.04)	7.50 (0.10)	1.68	N				
CGCG448-020_W	20h57m24.0s +17d07m35.1s	(-11.9)	20h57m24.0s +17d07m35.2s	(-95.6)	0.48 (0.01)	-0.42 (0.02)	9.14 (0.04)	—	c	3			

Source Name	Short-Low RA/DEC [J2000]	(PA) [°]	Long-Low RA/DEC [J2000]	(PA) [°]	6.2 μ m EQW [μ m]	sg _{7.7μm} (σ)	$F_{\nu}[30\mu\text{m}]/F_{\nu}[15\mu\text{m}](\sigma)$	Scale Factor	Merger Stage	MS (HST)
CGCG448-020_E	20h57m24.3s +17d07m39.1s	(-11.9)	20h57m24.3s +17d07m39.2s	(-95.6)	0.27 (0.01)	-0.92 (0.03)	9.82 (0.04)	—	c	3
IRAS20551-4250	20h58m26.8s -42d39m01.7s	(162.1)	20h58m26.7s -42d39m02.8s	(78.4)	0.10 (0.01)	-2.52 (0.10)	7.59 (0.02)	1.04	d	5
ESO286-G035	21h04m11.1s -43d35m34.4s	(-27.5)	21h04m11.1s -43d35m34.4s	(-111.2)	0.69 (0.01)	-0.24 (0.03)	7.02 (0.09)	1.43	a	
IRAS21101+5810	21h11m29.3s +58d23m07.6s	(10.5)	21h11m29.3s +58d23m07.6s	(-73.2)	0.55 (0.02)	-0.87 (0.07)	11.06 (0.15)	1.04	c	2
ESO343-IG013_S	21h36m10.5s -38d32m42.4s	(-31.9)	21h36m10.5s -38d32m42.4s	(-115.6)	0.61 (0.01)	-0.09 (0.03)	9.21 (0.18)	—	c	
ESO343-IG013_N	21h36m10.9s -38d32m32.6s	(-1.9)	21h36m10.9s -38d32m32.6s	(-115.6)	0.47 (0.01)	-0.48 (0.02)	6.71 (0.07)	—	c	
NGC7130	21h48m19.6s -34d57m01.9s	(154.1)	21h48m19.5s -34d57m02.1s	(70.4)	0.30 (0.01)	-0.27 (0.03)	5.67 (0.03)	1.42	N	
ESO467-G027	22h14m39.9s -27d27m51.4s	(-36.7)	22h14m39.9s -27d27m51.3s	(-120.4)	0.62 (0.01)	0.29 (0.02)	5.48 (0.09)	2.24	N	
IC5179	22h16m09.0s -36d50m38.1s	(121.5)*	22h16m09.3s -36d50m33.8s	(115.9)*	0.63 (0.01)	0.07 (0.02)	5.42 (0.02)	2.43	N	
ESO602-G025	22h31m25.5s -19d02m04.0s	(-31.4)	22h31m25.4s -19d02m04.0s	(-117.1)	0.45 (0.01)	-0.66 (0.04)	6.23 (0.08)	1.17	N	
UGC12150	22h41m12.2s +34d14m56.9s	(-20.1)	22h41m12.2s +34d14m56.8s	(-98.7)	0.53 (0.01)	-0.42 (0.02)	8.14 (0.09)	1.27	N	
ESO239-IG002	22h49m39.8s -48d50m58.4s	(-48.3)	22h49m39.8s -48d50m58.4s	(-132.0)	0.45 (0.02)	-0.49 (0.04)	10.35 (0.12)	1.08	d	5
IRASF22491-1808	22h51m49.4s -17d52m24.5s	(155.2)	22h51m49.2s -17d52m24.8s	(71.5)	0.48 (0.02)	-1.04 (0.13)	17.63 (0.33)	1.14	d	4
NGC7469	23h03m15.6s +08d52m26.2s	(-29.7)	23h03m15.6s +08d52m27.3s	(-113.4)	0.23 (0.002)	0.06 (0.02)	4.81 (0.03)	1.12	a	2
CGCG453-062	23h04m56.5s +19d33m07.6s	(-24.9)	23h04m56.6s +19d33m07.8s	(-103.6)	0.58 (0.02)	-0.46 (0.04)	12.83 (0.10)	1.50	N	
ESO148-IG002	23h15m47.0s -59d03m17.0s	(136.3)	23h15m47.0s -59d03m18.4s	(52.6)	0.31 (0.01)	-0.66 (0.03)	6.49 (0.05)	1.03	c	4
IC5298	23h16m00.7s +25d33m24.4s	(-19.5)	23h16m00.7s +25d33m24.5s	(-103.3)	0.12 (0.004)	-0.37 (0.02)	7.41 (0.02)	1.01	N	0
NGC7552	23h16m10.6s -42d35m03.8s	(112.9)*	23h16m10.6s -42d35m05.8s	(107.8)*	0.56 (0.01)	-0.21 (0.02)	6.62 (0.01)	1.72	N	
NGC7591	23h18m16.3s +06d35m08.7s	(-27.4)	23h18m16.2s +06d35m09.2s	(-109.7)	0.48 (0.01)	-0.37 (0.05)	7.96 (0.13)	1.21	N	
NGC7592_W	23h18m21.7s -04d24m57.6s	(119.1)*	23h18m21.5s -04d24m54.2s	(112.9)*	0.30 (0.01)	-1.08 (0.03)	5.13 (0.02)	1.10	b	
NGC7592_E	23h18m22.7s -04d24m57.8s	(119.1)*	23h18m22.8s -04d25m02.3s	(112.9)*	0.69 (0.01)	0.11 (0.02)	8.38 (0.07)	1.20	b	2
ESO077-IG014_W	23h21m03.7s -69d13m00.9s	(-55.8)	23h21m03.7s -69d13m00.9s	(-139.5)	0.63 (0.01)	-0.59 (0.04)	11.84 (0.17)	—	b	2
ESO077-IG014_E	23h21m05.4s -69d12m47.2s	(-55.8)	23h21m05.4s -69d12m47.2s	(-139.5)	0.49 (0.01)	-0.61 (0.03)	12.54 (0.12)	—	b	2
NGC7674	23h27m56.7s +08d46m44.5s	(116.5)*	23h27m56.6s +08d46m41.8s	(20.5)*	0.02 (0.01)	-0.13 (0.02)	2.52 (0.02)	1.13	a	2
NGC7679	23h28m46.6s +03d30m41.7s	(-27.4)	23h28m46.6s +03d30m41.7s	(-111.1)	0.64 (0.01)	0.34 (0.02)	5.78 (0.06)	1.41	a	
IRASF23365+3604	23h39m01.3s +36d21m10.2s	(-35.5)	23h39m01.4s +36d21m11.3s	(-119.2)	0.41 (0.02)	-1.41 (0.17)	10.04 (0.11)	1.89	d	5
MCG-01-60-022	—	—	23h42m00.7s -03d36m54.7s	(-114.0)	—	—	7.24 (0.13)	—	a	
IRAS23436+5257	23h46m05.4s +53d14m01.3s	(-3.9)	23h46m05.4s +53d14m01.3s	(-87.7)	0.37 (0.01)	-0.22 (0.03)	7.00 (0.06)	1.24	c	4
Arp86_S	23h46m58.5s +29d27m31.6s	(-19.8)	23h46m58.5s +29d27m31.8s	(-103.5)	0.72 (0.01)	0.12 (0.02)	6.14 (0.11)	1.61	b	
Arp86_N	23h47m04.8s +29d28m59.6s	(-19.7)	23h47m04.8s +29d28m59.8s	(-103.5)	0.32 (0.01)	0.14 (0.04)	6.72 (0.18)	1.53	b	

Source Name	Short-Low RA/DEC [J2000]	(PA) [°]	Long-Low RA/DEC [J2000]	(PA) [°]	6.2 μ m EQW(σ) [μ m]	$s_{9.7\mu\text{m}}$ (σ)	$F_{\nu}[30\mu\text{m}]/F_{\nu}[15\mu\text{m}]$ (σ)	Scale Factor	Merger Stage	MS (HST)
NGC7771_W	23h51m04.0s +20d09m02.0s	(-19.8)	23h51m04.0s +20d09m02.0s	(-103.6)	0.39 (0.01)	0.27 (0.06)	6.26 (0.11)	1.34	N	
NGC7771_S	23h51m22.5s +20d05m47.0s	(-19.8)	23h51m22.5s +20d05m47.0s	(-103.6)	0.36 (0.01)	-0.20 (0.04)	4.42 (0.05)	2.11	c	
NGC7771_LN	23h51m24.9s +20d06m43.0s	(-19.8)	23h51m24.9s +20d06m43.1s	(-103.6)	0.52 (0.01)	-0.24 (0.03)	8.43 (0.04)	1.95	a	
MRK0331	23h51m26.7s +20d35m10.1s	(-19.6)	23h51m26.7s +20d35m10.3s	(-103.3)	0.63 (0.01)	-0.35 (0.03)	9.40 (0.05)	1.19	a	1

MIR Spectral Parameters of the GOALS Sample. Column (1): Source Name, Columns (2)-(5): the central right ascension, declination, and position angle of the field of view for the SL and LL observations (for staring mode data: RA_FOV, DEC_FOV, & PA_FOV from the headers with a pointing accuracy within 1''; for mapping mode data: calculated from the four corners of the extraction aperture used in CUBISM), Column (6): the equivalent width of the 6.2 μ m PAH feature in μ m, Column (7): the apparent depth of the 9.7 μ m silicate absorption feature, Column (8): the MIR slope calculated using F_{ν} at 15 and 30 μ m, Column (9): the SL-to-LL scale factor, Column (10): the merger stage (N = nonmerger, a = pre-merger, b = early stage merger, c = mid-stage merger, and d = late stage merger, see Section 2.5 for details), and Column (11): merger stage as derived from the high resolution HST data (0 = nonmerger, 1 = pre-merger, 2 = ongoing merger with separable progenitor galaxies, 3 = ongoing merger with progenitors sharing a common envelope, 4 = ongoing merger with double nuclei plus tidal tail, 5 = post-merger with single nucleus plus prominent tail, and 6 = post-merger with single nucleus with disturbed morphology, as described in Haan et al. (2011)).

*Data was taken in mapping mode, and so the PA was user-selected.